РОССИЙСКИЙ ГОСУДАРСТВЕННЫЙ ПЕДАГОГИЧЕСКИЙ УНИВЕРСИТЕТ им. А. И. ГЕРЦЕНА
HERZEN STATE PEDAGOGICAL UNIVERSITY of RUSSIA

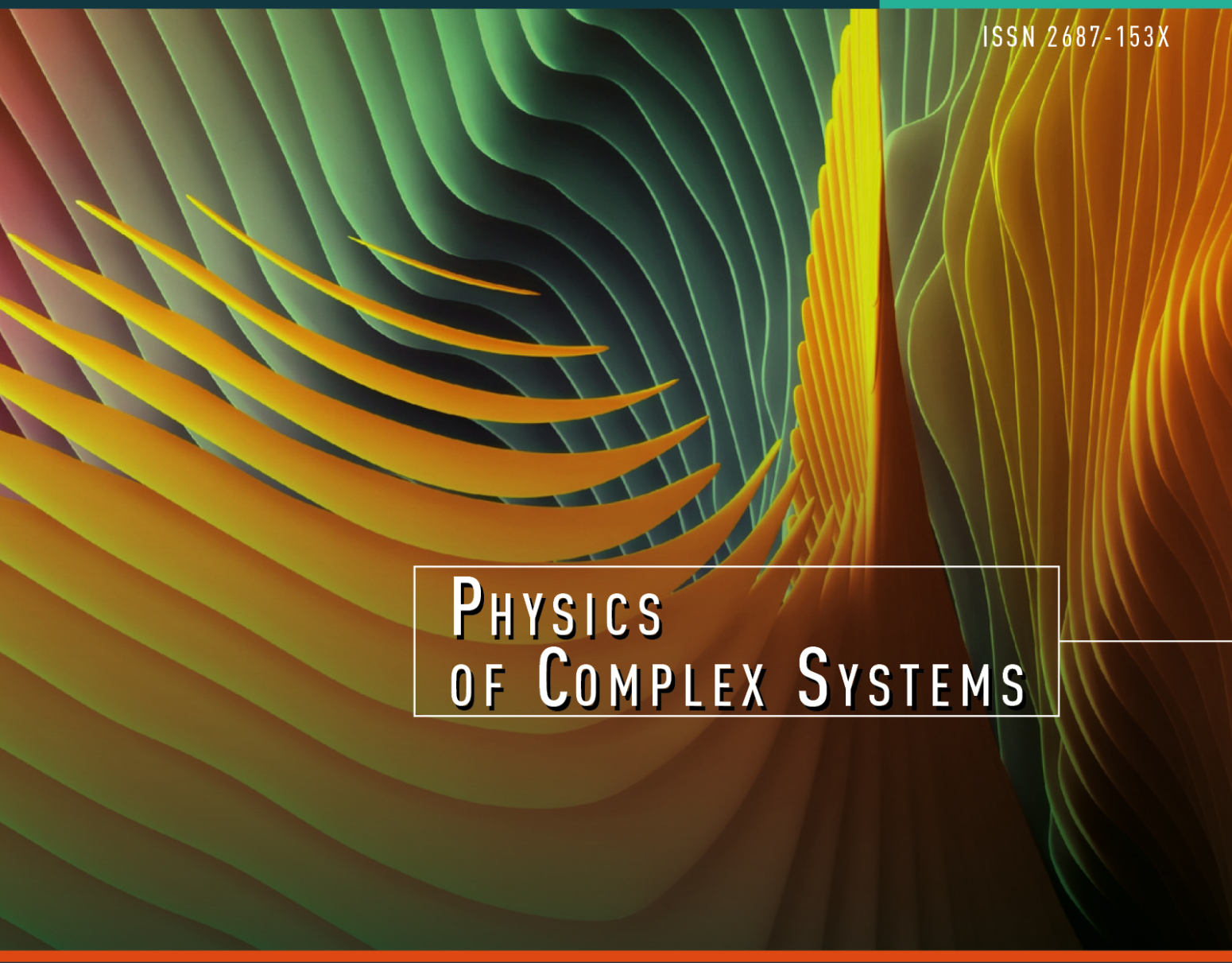

ISSN 2687-153X

Physics of Complex Systems

Т. 2 № 1 2021

Vol. 2 No. 1 2021

Herzen State Pedagogical University of Russia

ISSN 2687-153X (online)
physcomsys.ru
https://www.doi.org/10.33910/2687-153X-2021-2-1
2021. Vol. 2, no. 1

PHYSICS OF COMPLEX SYSTEMS

Mass Media Registration Certificate El No. FS77-77889, issued by Roskomnadzor on 10 February 2020
Peer-reviewed journal
Open Access
Published since 2020
4 issues per year

Publishing house of Herzen State Pedagogical University of Russia
48 Moyka Emb., St Petersburg 191186, Russia
E-mail: izdat@herzen.spb.ru
Phone: +7 (812) 312-17-41

Data size 6,53 Mbyte
Published at 29.03.2021

Editors of the English text *M. V. Gorodisky, I. A. Nagovitsyna*
Cover design by *O. V. Rudneva*
Layout by *A. M. Khodan, L. N. Kliuchanskaya*

CONTENTS

Condensed Matter Physics. Dielectric Physics

UDC 538.9

https://www.doi.org/10.33910/2687-153X-2021-2-1-3-8

Thermal quenching of luminescence in $(Lu,Gd,Y)_3(Ga, Al)_5O_{12}$:Ce complex garnet ceramics at high and low temperatures

P. A. Rodnyi[1], I. D. Venevtsev✉[1], V. M. Khanin[2]

[1] Peter the Great Saint Petersburg Polytechnic University, 29 Polytechnicheskaya Str., Saint Petersburg 195251, Russia
[2] Delft University of Technology, 15 Mekelweg, 2629 JB Delft, the Netherlands

Authors

Piotr A. Rodnyi, ORCID: 0000-0001-7213-3855

Ivan D. Venevtsev, ORCID: 0000-0002-9420-0278, e-mail: Venevtsev.Ivan@gmail.com

Vasilii M. Khanin, ORCID: 0000-0001-6399-1540

For citation: Rodnyi, P. A., Venevtsev, I. D., Khanin, V. M. (2021) Thermal quenching of luminescence in $(Lu,Gd,Y)_3(Ga, Al)_5O_{12}$:Ce complex garnet ceramics at high and low temperatures. *Physics of Complex Systems*, 2 (1), 3–8. https://www.doi.org/10.33910/2687-153X-2021-2-1-3-8

Received 15 December 2020; reviewed 23 December 2020; accepted 23 December 2020.

Abstract. Cerium-doped complex garnets with the general formula $(Lu,Y,Gd)_3,(Ga,Al)_5O_{12}$:Ce are promising materials to be used in PET and CT scanners. By modifying garnet composition (bandgap engineering), one can adjust its scintillation properties to fit a specific set of requirements. In certain compositions, Ce^{3+} luminescence intensity can decrease upon cooling (negative thermal quenching). The reason for that is still a matter of active debate. This article is focused on negative thermal quenching in Ce-doped $(Lu,Gd)_3(Ga,Al)_5O_{12}$ garnet ceramics. We have measured thermally stimulated luminescence, temperature dependence of the X-ray excited luminescence intensity, and other scintillation properties of samples which have different Lu and Ga content and were annealed in different conditions. We discuss that negative thermal quenching in our samples can be attributed to the process of charge carrier localization on traps at lower temperatures.

Keywords: complex garnet ceramics, Ce-doping, annealing, radioluminescence spectra, negative thermal quenching, thermal ionization.

Introduction

Cerium-doped complex garnets with the general formula $(Lu,Gd,Y)_3(Ga, Al)_5O_{12}$:Ce are very promising materials to be used as scintillators (Ronda et al. 2016) and persistent phosphors (Ueda, Tanabe 2019). This class of materials is actively studied by many research teams (Nikl, Yoshikawa 2019; Ueda, Dorenbos, Bos, Kuroishi et al. 2015). The interest of researchers is stirred by the need to improve the scintillation properties of complex garnets used in medical tomography (Wieczorek et al. 2020). The available studies usually focus on the energy resolution and timing performance of scintillators. However, it is also important to study temperature stability of their luminescence properties, since that is one of the key requirements for practical applications. Scintillation detectors used in computer or positron emission tomography scanners are exposed to heat which emanates from high voltage electronics, moving mechanical parts, etc. A change in the temperature of the detector causes a change in its main properties—i.e., light output and decay time (Venevtsev et al. 2017). A reliable operation of PET or CT scanners requires scintillation detectors to be minimally affected by temperature variations. Thermal stability can be ensured by the selection of the optimal chemical composition of the scintillator, which requires a detailed study of the physical processes occurring in scintillators.

In the current work, we study the temperature dependence of the main properties of $(Lu,Gd,Y)_3(Ga,Al)_5O_{12}$:Ce scintillators. We specifically focus on the least studied low-temperature region, where negative thermal quenching (NTQ) has been observed.

In our previous research, we have been able to show several examples of garnet compositions in which NTQ takes place. In $(Gd,Y)_3Al_5O_{12}$:Ce (Venevtsev et al. 2017), NTQ is very pronounced in a wide range of temperatures from 90 to 450 K, especially in the basic YAG:Ce composition. Those results have shown that although Gd has a significant influence on Ce emission intensity, it does not directly participate in NTQ. Gd^{3+} ions have an emission line at 311 nm which can overlap with Ce^{3+} $4f \rightarrow 5d_2$ excitation band around 300–400 nm resulting in an efficient resonant energy transfer. This overlap increases at higher temperatures due to broadening of Ce^{3+} excitation bands, which potentially can lead to an increased Ce^{3+} emission intensity when the sample is heated up. However, this transition has been shown to occur and early saturate at very low temperatures, between 30 and 70 K (Bartosiewicz et al. 2015) with no significant changes at higher temperatures. Our earlier work (Venevtsev et al. 2017) has also shown that in the range from 90 to 400 K (where significant portion of NTQ of Ce^{3+} emission takes place) there is no change in the intensity of left-over Gd^{3+} lines.

An alternative explanation is that upon cooling the localization of charge carriers on traps is occurring more efficiently due to a decrease in the mobility of carriers and increase of their lifetime on traps (Zych et al. 2000).

Experimental methods

All tested samples were prepared at the Philips Research Eindhoven facility in the form of ceramic disks 2 mm thick and 15 mm in diameter. To study the influence of Ga content on the NTQ, a set of ceramics with the composition $Y_2Gd_1Ga_xAl_{5-x}O_{12}$:$Ce^{3+}$ (x = 2.0, 2.5, and 3.0) was used. Three other samples of $Lu_xGd_{3-x}Ga_2Al_3O_{12}$:$Ce^{3+}$ (x = 0.0, 0.3, and 1.0) were used to study the impact of Lu content on the temperature quenching under X-ray irradiation. Additional two samples included ceramics of $Lu_{0.33}Gd_{2.67}Ga_{2.5}Al_{2.5}O_{12}$:$Ce^{3+}$ annealed in wet forming gas (FG) and air (O_2).

Radioluminescence (RL) spectra were measured under continuous excitation using an X-ray tube with tungsten anode. The tube voltage and current were 40 kV and 10 mA, respectively. Emission was detected by an MDR-2 monochromator coupled to a Hamamatsu H8259-01 photon counting head. Samples were positioned in reflection geometry (Potapov et al. 2004).

Temperature-dependent measurements were carried out using a vacuum cryostat. A copper sample holder and silver glue (Leitsilber 200) were used for better thermal conductivity. The temperature dependence of RL intensity for each sample was measured at a fixed wavelength corresponding to the maximum of Ce^{3+} emission.

Thermally stimulated luminescence (TSL) measurements were performed in a following way: samples were irradiated with X-rays for 300 s at 77–80 K (using the same X-ray tube), followed by a 600s waiting time to diminish the influence of thermally active traps; then measurements of TSL intensity were carried out under a constant heating rate of 0.25 K/s using the Hamamatsu H8259 photon counting head in the integration mode. The temperature lag at such speed did not exceed 5 K, a value comparable to the overall error of the temperature measurements.

Results and discussion

To reveal a correlation between negative thermal quenching and charge localization processes we performed series of RL and TSL measurements. Temperature dependence of Ce^{3+} emission for a set of three ceramic samples of $Y_2Gd_1Ga_xAl_{5-x}O_{12}$:Ce with Ga content of x = 2.0, 2.5 and 3.0 is shown in Fig.1a (normalized at maximum). All three ceramic samples contain the usual high-temperature thermal quenching region as well as the negative thermal quenching region. The position of emission maximum changes with Ga content and is 320, 250 and 210 K for x = 2.0, 2.5, and 3.0, respectively.

It has been shown in multiple works (Ogieglo et al. 2013; Ueda et al. 2015) that at high temperatures the decrease in Ce^{3+} emission intensity is attributed to thermal ionization of an electron from Ce^{3+} excited states. The fact that with the increase of Ga content we observe a low temperature shift in the position of the high-temperature quenching region indicates the lowering of the bottom of the conduction band (CB).

 https://www.doi.org/10.33910/2687-153X-2021-2-1-3-8

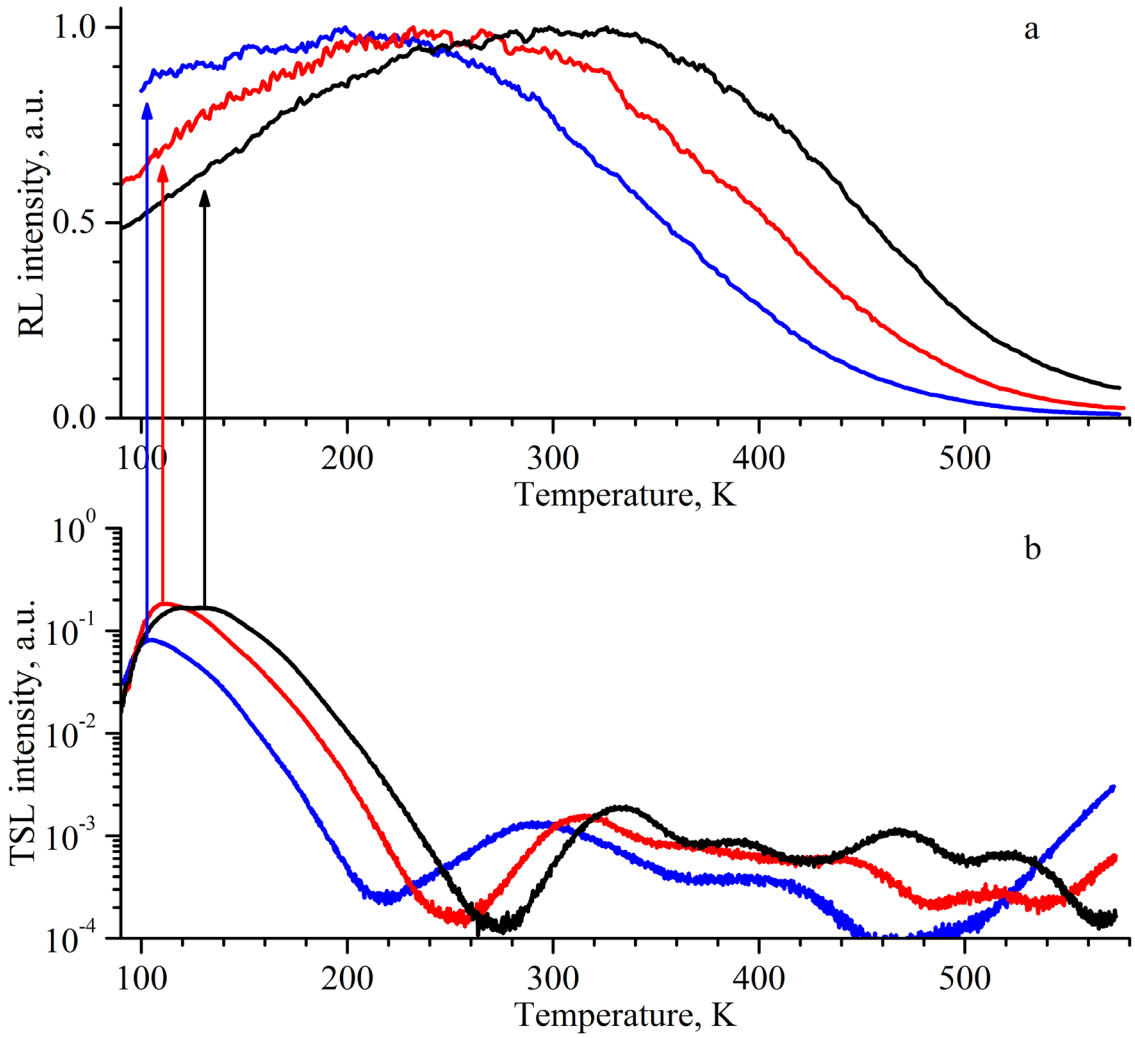

Fig. 1. Temperature dependences of RL intensity (a) and thermally stimulated luminescence (b) of $Y_2Gd_1Ga_xAl_{5-x}O_{12}:Ce^{3+}$ ceramics with x = 2.0 (black line), 2.5 (red line) and 3.0 (blue line)

NTQ in these samples takes place in the range from 90 to 300, 220 and 200 for ceramics with X = 2.0, 2.5, and 3.0, respectively. Furthermore, the slope of the negative thermal quenching region clearly decreases. Such behavior can be explained with the use of TSL measurements which are meant to point at the presence of thermally active traps at a certain temperature and, in some cases, to estimate the trap depth. TSL curves are shown in Fig. 1b in the same temperature range. Every curve consists of a large peak around 90–220 K, which could also be the combination of several unresolved peaks, and a set of smaller peaks at higher temperature. It is known that the latter can be attributed to various rare-earth and transition metal impurities, such as Yb, Eu, Cr, V, etc. (Dorenbos et al. 2015a; Khanin et al. 2017). The low-temperature TSL structure is usually attributed to various intrinsic defects, such as antisites or vacancies (Fasoli et al. 2011). Changes in garnet composition led to either a decrease or increase in the depth of related traps relative to the bottom of the conduction band and, consequently, to a shift of the peak maxima at the temperature scale.

In Fig. 1b, we can clearly see that positions of the largest peaks at low temperature correlate with the shape of the NTQ in Fig. 1a. For example, in $Y_2Gd_1Ga_2Al_3O_{12}:Ce$ ceramics the TSL peak is located around 90–240 K, and the corresponding NTQ range is approximately the same. In $Y_2Gd_1Ga_2Al_3O_{12}:Ce$, this peak has a lower intensity and is shifted to 90–180 K range while the corresponding NTQ curve has a flatter slope and also spans over the same range of temperatures.

Fig. 2a demonstrates temperature dependence of Ce^{3+} emission intensity in $Lu_xGd_{3-x}Ga_2Al_3O_{12}:Ce^{3+}$ (x = 0.0, 0.3, and 1.0). In this case, we did not observe the shift in the thermal ionization process,

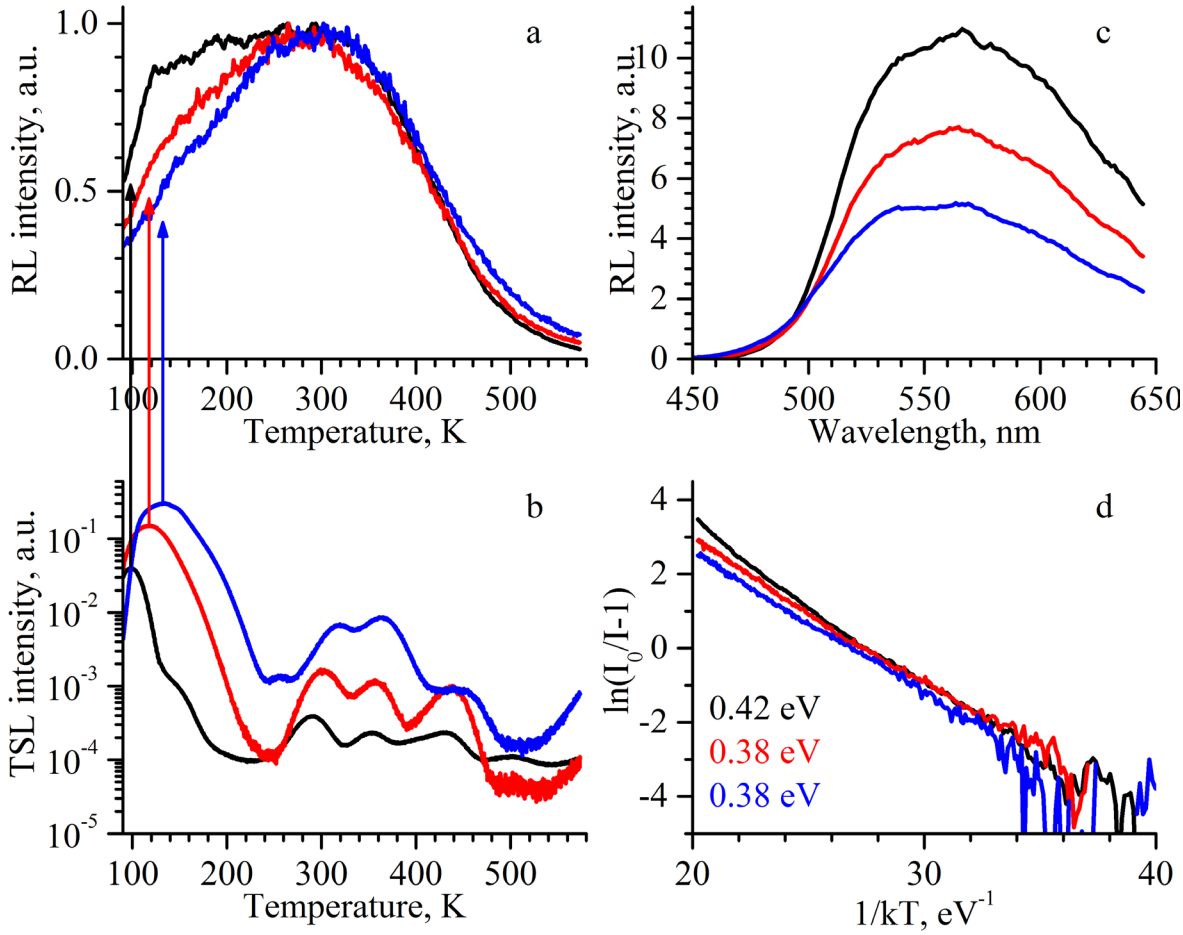

Fig. 2. Properties of $Lu_xGd_{3-x}Ga_2Al_3O_{12}:Ce^{3+}$ ceramics with x = 0.0 (black line), 0.3 (red line) and 1.0 (blue line), where a—temperature dependence of RL intensity, b—thermally stimulated luminescence curves, c—RL spectra at room temperature, d—Arrhenius plots of RL temperature dependence

except for the slight change in the shape of the slope at higher temperatures. The emission maximum is located at 300 K for all samples, which ensures the best thermal stability for room temperature applications. Below 300 K, the ceramic samples behave differently. In case no Lu is present, we observe a slow decrease in intensity in the range from 300 to ~125 K followed by a sharp drop in intensity in the range from 125 to 90 K. The samples which contain Lu have an overall steeper slope with no sharp drop. At 90 K, ceramics with x = 1 has the lowest emission intensity.

TSL curves of the samples are shown in Fig. 2b. The peak structure is similar to what was observed in Fig. 1b. In this case, we can find the same patterns: at Lu x = 1.0, the NTQ spans from 90 to 240 K, while the first TSL peak has the range from 90 to around 230 K; at Lu x = 0.3, the NTQ has a slightly flatter slope and spans up to around 200 K, while the corresponding TSL peak has a decreased intensity and a range from 90 to 190 K. The most interesting picture is observed for the ceramic sample with Lu x = 0.0: in the range from ~115 to 190 K, it has a significantly smaller TSL intensity than the other samples and, at the same time, the intensity of Ce emission barely changes in that region; but at lower temperature (from 115 to 90 K) there is still an intensive TSL peak that, most probably, corresponds to traps which are responsible for the sudden drop in intensity.

We also made an attempt to determine the activation energy of thermal ionization process. This is illustrated by the Arrhenius plot in Fig. 2d. The plot corresponds to the range from 290 to 580 K. As these curves were measured at Ce^{3+} emission maximum (Fig. 2c), their shape is determined only by the processes related to energy transfer to Ce ions. The linear shape indicates that there is a single thermally activated process. The activation energy can be determined by the linear approximation where the slope is the desired value (also shown in Fig. 2d). It is clearly seen that the addition of Lu has only a slight effect on the activation energy. Since Ce 4*f* ground state position in the energy diagram does not

 https://www.doi.org/10.33910/2687-153X-2021-2-1-3-8

depend on the composition (Dorenbos 2013) and since the distances from the ground to the excited state and from the excited state to the bottom of the CB also stay almost the same, we can conclude that the position of the CB bottom does not significantly change upon addition of Lu up to x = 1. Therefore, changes in the shape of the TSL and, consequently, of the NTQ are due to the change in the concentration of traps. This is most probably explained by the absence of Lu in $Gd_3Ga_2Al_3O_{12}:Ce^{3+}$ which led to disappearance of certain types of antisites.

To further investigate the influence of trap concentration on the shape of the NTQ, we used two $Lu_{0.33}Gd_{2.67}Ga_{2.5}Al_{2.5}O_{12}:Ce^{3+}$ ceramic samples prepared under exactly the same conditions but annealed in different atmospheres—i.e., wet FG and O_2. It is known that treatment in an oxidizing atmosphere can improve luminescence properties of multicomponent garnets and decrease their afterglow and TSL intensity (Boka et al. 2015). In our study, the intensity of Ce^{3+} luminescence of O_2 annealed ceramic (Fig. 3c) is around 40% lower than that of wet FG annealed sample. On the other hand, Fig. 3b shows that the improvement of the TSL response does take place. Both samples have a similar shape of the TSL curve with the main peak around 90–200 K, but the sample which was treated in O_2 has around 1000 times lower intensity. At the same time, temperature dependence of the RL intensity of that sample (Fig. 3a) has a much less pronounced NTQ region. Such correlation is another indirect evidence that NTQ occurs as a result of localization of charge electrons on traps.

The visible two-slope behavior of the luminescence intensity in the high temperature region in Fig. 3a is a notable aspect of these samples. One of the two components located at higher temperature has an activation energy E_1 = 0.38 eV and basically corresponds to the thermal depth of the Ce^{3+} $5d_1$ excited state relative to the conduction band (the approximation is shown in Fig. 3d), while the other one (between 120 and 300 K) can be attributed to the process of thermally activated transfer of an electron to a nearby trap (Grigorjeva et al. 2018).

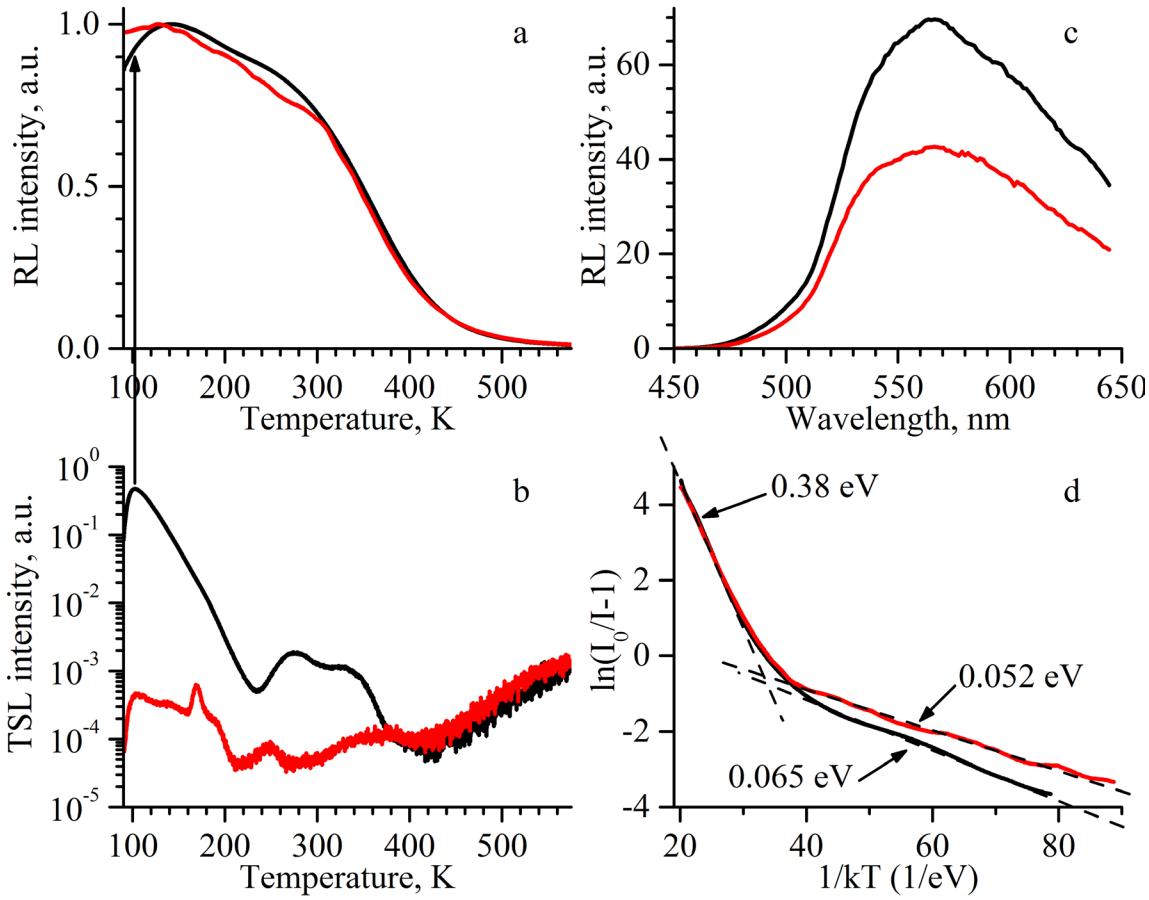

Fig. 3. Properties of $Lu_{0.33}Gd_{2.67}Ga_{2.5}Al_{2.5}O_{12}:Ce^{3+}$ ceramics annealed in wet FG (black line) and O2 (red line), where a—temperature dependence of RL intensity, b—thermally stimulated luminescence curves, c—RL spectra at room temperature, d—Arrhenius plots of RL temperature dependence

Conclusion

Our studies have shown several instances of negative thermal quenching in Ce-doped complex garnets. In all the instances, there was a distinct correlation between the position of low-temperature TSL peaks and the location of the NTQ in the corresponding RL temperature dependence. Changes in the TSL intensity also affected the slope of the NTQ by making it steeper where the corresponding peak is higher and vice versa. Additionally, a different temperature behavior was observed in two ceramic samples which had the same composition and, therefore, were expected to display only a minimal difference between energy transfer processes. These observations have led us to a conclusion that the negative thermal quenching of Ce^{3+} radioluminescence in complex garnet compounds can be attributed to the localization of charge carriers on traps at low temperatures.

References

Bartosiewicz, K., Babin, V., Kamada, K. et al. (2015) Energy migration process in undoped and Ce-doped multicomponent garnet single crystal scintillators. *Journal of Luminescence*, 166, 117–122. https://www.doi.org/10.1016/j.jlumin.2015.05.015 (In English)

Boka, J., Horodysky, P., Krzyžánek, V. (2015) Effect of oxidation annealing on optical properties of YAG:Ce single crystals. *Optical Materials*, 46, 591–595. https://www.doi.org/10.1016/j.optmat.2015.05.035 (In English)

Dorenbos, P. (2013) Electronic structure and optical properties of the lanthanide activated $RE_3(Al_{1-x}Ga_x)_5O_{12}$ (RE=Gd, Y, Lu) garnet compounds. *Journal of Luminescence*, 134, 310–318. https://www.doi.org/10.1016/j.jlumin.2012.08.028 (In English)

Fasoli, M., Vedda, A., Nikl, M. et al. (2011) Band-gap engineering for removing shallow traps in rare-earth $Lu_3Al_5O_{12}$ garnet scintillators using Ga^{3+} doping. *Physical Review B*, 84, article 081102. https://www.doi.org/10.1103/PhysRevB.84.081102 (In English)

Grigorjeva, L., Kamada, K., Nikl, M. et al. (2018) Effect of Ga content on luminescence and defects formation processes in $Gd_3(Ga,Al)_5O_{12}$:Ce single crystals. *Optical Materials*, 75, 331–336. https://www.doi.org/10.1016/j.optmat.2017.10.054 (In English)

Khanin, V., Venevtsev, I., Spoor, S. et al. (2017) A new method for unambiguous determination of trap parameters from afterglow and TSL curves connection: Example on garnets. *Optical Materials*, 72, 161–168. https://www.doi.org/10.1016/j.optmat.2017.05.040 (In English)

Nikl, M., Yoshikawa, A. (2015) Recent R&D trends in inorganic single crystal scintillator materials for radiation detection. *Advanced Optical Materials*, 3 (4), 463–481. https://www.doi.org/10.1002/adom.201400571 (In English)

Ogieglo, J. M., Katelnikovas, A., Zych, A. et al. (2013) Luminescence and luminescence quenching in $Gd_3(Ga,Al)_5O_{12}$ scintillators doped with Ce^{3+}. *The Journal of Physical Chemistry A*, 117 (12), 2479–2484. https://www.doi.org/10.1021/jp309572p (In English)

Potapov, A. S., Rodnyi, P. A., Mikhrin, S. B. (2004) Experimental set-up for measurement of luminescence characteristics at X-ray excitation. *Radiation Measurements*, 38 (4–6), 839–842. https://www.doi.org/10.1016/j.radmeas.2004.02.007 (In English)

Ronda, C., Wieczorek, H., Khanin, V., Rodnyi, P. (2016) Review-scintillators for medical imaging: A tutorial overview. *ECS Journal of Solid State Science and Technology*, 5 (1), R3121–R3125. https://www.doi.org/10.1149/2.0131601jss (In English)

Ueda, J., Dorenbos, P., Bos, A. J. J., Kuroishi, K. et al. (2015) Control of electron transfer between Ce^{3+} and Cr^{3+} in the $Y_3Al_{5-x}Ga_xO_{12}$ host *via* conduction band engineering. *Journal of Materials Chemistry C*, 3 (22), 5642–5651. https://www.doi.org/10.1039/C5TC00546A (In English)

Ueda, J., Dorenbos, P., Bos, A. J. J., Meijerink, A. et al. (2015) Insight into the thermal quenching mechanism for $Y_3Al_5O_{12}$:Ce^{3+} through thermoluminescence excitation spectroscopy. *The Journal of Physical Chemistry C*, 119 (44), 25003–25008. https://www.doi.org/10.1021/acs.jpcc.5b08828 (In English)

Ueda, J., Tanabe, S. (2019) Review of luminescent properties of Ce^{3+}-doped garnet phosphors: New insight into the effect of crystal and electronic structure. *Optical Materials: X*, 1, article 100018. https://www.doi.org/10.1016/j.omx.2019.100018 (In English)

Venevtsev, I., Khanin, V., Rodnyi, P. et al. (2017) Temperature dependence of photo- and radioluminescence of $(Gd,Y)_3Al_5O_{12}$:Ce^{3+} mixed oxide garnet ceramics. In: *PIERS: 2017 Progress in Electromagnetics Research Symposium-Spring: Proceedings: 22–25 May 2017, St. Petersburg, Russia*. New York: IEE Publ., pp. 2633–2636. (In English)

Wieczorek, H., Khanin, V., Ronda, C. et al. (2020) Band gap variation and trap distribution in transparent garnet scintillator ceramics. *IEEE Transactions on Nuclear Science*, 67 (8), 1934–1945. https://www.doi.org/10.1109/TNS.2020.3001303 (In English)

Zych, E., Brecher, C., Glodo, J. (2000) Kinetics of cerium emission in a YAG:Ce single crystal: The role of traps. *Journal of Physics: Condensed Matter*, 12 (8), 1947–1958. https://www.doi.org/10.1088/0953-8984/12/8/336 (In English)

Physics of Semiconductors.
Semiconductor Physics

UDC 537.311 https://www.doi.org/10.33910/2687-153X-2021-2-1-9-14

Luminescence of insulator layers on silicon excited by electrons

A. P. Baraban[1], V. A. Dmitriev✉[1]

[1] Saint-Petersburg State University, 7/9 Universitetskaya Emb., Saint-Petersburg 199034, Russia

Authors

Alexander P. Baraban, ORCID: 0000-0001-8745-7019

Valentin A. Dmitriev, ORCID: 0000-0003-3604-9490, e-mail: esssec@gmail.com

For citation: Baraban, A. P., Dmitriev, V. A. (2021) Luminescence of insulator layers on silicon excited by electrons. *Physics of Complex Systems*, 2 (1), 9–14. https://www.doi.org/10.33910/2687-153X-2021-2-1-9-14

Received 11 December 2020; reviewed 20 December 2020; accepted 21 December 2020.

Funding: This work was performed using the equipment of Saint Petersburg State University Research Park, in particular, the Interdisciplinary Resource Center for Nanotechnology and the Center for Innovative Technologies of Composite Nanomaterials.

Abstract. We present a comparative analysis of cathodoluminescence (CL) and electroluminescence (EL) spectra measured on Si–SiO_2 and Si–Ta_2O_5 structures with various thicknesses of insulator layers. Spectral distribution of luminescence depends on how the insulator layer was formed, its thickness and type of excitation. The analysis indicates that CL and EL spectra of Si–SiO_2 structures, grown by thermal oxidation of silicon in "dry" oxygen, are almost identical in spectral composition. Based on the dependence of intensity of the luminescence band with a maximum at energy of 2.2 eV, it was concluded that the corresponding luminescence centers are uniformly distributed over the oxide layer thickness in the range of 30–200 nm. It is assumed that these luminescence centers are oxygen vacancies formed during the thermal oxidation of silicon. In the case of Ta_2O_5 layers on silicon, the presence of defects (luminescence centers) in the oxide layer leads to the formation of a set of energy levels in the band gap of the Ta_2O_5 layers obtained by ALD. They appear in the luminescence spectra regardless of the excitation method.

Keywords: cathodoluminescence, electroluminescence, molecular layer deposition, spectral distribution, electronic structure, luminescence centers.

Introduction

Luminescence is widely used in fundamental studies of solids, including semiconductor-insulator structures (Baraban, Samarin et al. 2019; Coenen, Haegel 2017; Yacobi, Holt 1990; Zamoryanskaya, Sokolov 1998). Their luminescent properties of interest to researchers because of their potential applications in silicon-based optoelectronic devices. For this reason, our major focus on electroluminescence (EL) and cathodoluminescence (CL) in silicon-insulator structures.

The study compares the results obtained by two methods of luminescence excitation. Our aim was to secure additional information through comprehensive analysis of aggregate luminescence data.

Experimental procedure

The study focused on Si-SiO_2 and Si-Ta_2O_5 structures. Essentially, the SiO_2 film was grown on a single-crystal silicon wafer of *p*-type ($N_A = 8 \times 10^{14}$ cm^{-3}) by thermal oxidation in dry oxygen at a temperature of 1000°C. The Ta_2O_5 layers were synthesized using a well-known molecular layer deposition method (a variant of the ALD method), which we previously used to synthesize dielectric layers in (Baraban, Dmitriev et al. 2019; Baraban et al. 2020). The Ta_2O_5 films were grown on single-crystalline silicon substrates (acceptor concentration of 3×10^{14} cm^{-3}) of 100 mm in diameter using two reagents, namely,

tantalum chloride and water. To achieve a high growth rate, the Si–Ta_2O_5 structures were synthesized on a rotating silicon substrateat a temperature in the range of 180–250°C with a tantalum chloride evaporator temperature of 45–90°C.

The obtained films were thoroughly investigated by SEM+EDX, TEM, XRD, CL and TDS methods in an attempt to understand their composition, inner structure and electronic properties. The thickness of the dielectric layers was determined on cleaved structures with the scanning helium ion microscope Zeiss ORION and monitored by ellipsometry at the wavelength of 632.8 nm.

To implement the CL method, we used the scanning electron microscope Zeiss SUPRA 40VP with the Gatan MonoCL3+ recording system. The CL spectra were recorded in the range of 250–800 nm while continuously scanning an electron beam over the sample surface. Each spectrum was recorded at a new location of the sample. The width of the scanning area was 30 microns, the acquisition time of one point of the spectrum was 1 s, the spectral resolution was 2 nm, incident electron energy was 5, 10, 15 keV, the beam current was 2–11 nA.

The EL spectra were recorded at a positive potential of the silicon substrate in the electrolyte-dielectric-semiconductor system in the range of 250–800 nm on an automated setup based on a wide-aperture monochromator (Czerny–Turner configuration) with one 600 l/mm diffraction grating under conditions that did not allow breakdown or degradation of the oxide layer (Baraban et al. 2009). An aqueous solution of Na_2SO_4 was used as an electrolyte.

All measurements were performed at a temperature of 293 K.

Results and discussion

Luminescence of SiO_2 layer excited by electrons (CL and EL)

In the cases of electroluminescence and cathodoluminescence of SiO_2 layers, low-energy electrons (energies below 10 eV) interact with defects (called Luminescence Centers (LC)) of the oxide layer that appear during oxide growth. In the case of CL, low energy electrons are produced by incident electrons in the volume of the oxide layer. The electron energy used in our experiments is enough to excite luminescence throughout the thickness of the whole oxide layer. In the case of EL, electrons are injected into the oxide layer from the field electrode (in this case, the spectrally transparent electrolyte). These electrons are subsequently accelerated (heated) in an electric field with a strength of more than 10 MV/cmin the 25 nm thick oxide layer energies (5–10 eV) sufficient to excite the luminescence centers (Baraban et al. 2009; Babaran et al. 1993). The excitation of EL, excited by hot electrons, occurs throughout the thickness of the oxide layer except a 25 nm layerand a tunnel-thin SiO_2 layer on the outer boundary of the structure (Baraban et al. 2009). The above consideration allows to use the same approach to analyze the results of CL and EL methods.

This is confirmed by the type of spectral distributions shown in Fig. 1 and Fig. 2A comprehensive analysis of the CL and EL spectra (for this method of oxide layer formation) allowed us to approximate them with a single set of Gaussian radiation bands, the maxima (and dispersions) of which corresponded to the energies in eV: 1.87 ± 0.04 (0.08 ± 0.01); 2.20 ± 0.05 (0.15 ± 0.04); 2.50 ± 0.08 (0.20 ± 0.06); 2.90 ± 0.08 (0.20 ± 0.06); 3.3 ± 0.1 (0.25 ± 0.8); 3.9 ± 0.1 (0.25 ± 0.06); 4.2 ± 0.1 (0.25 ± 0.08). Examples of such approximation are shown in Fig. 3. This result indicates the excitation of identical LC formed in the oxide layer during thermal oxidation.

It should be noted that when changing the method of oxide layer formation, the EL spectrum may be more informative (it allows to reliably select a larger number of characteristic radiation bands) than the CL spectrum, as shown in Fig. 4. In this case, the observed differences in the EL spectrum are due to the peculiarities of luminescence excitation by an electric field (Baraban et al. 2012).

The luminescence spectra of SiO_2 layers excited by electrons make it possible to distinguish the three most reliably recorded radiation bands, whose maxima are located at energies of 4.2 eV, 2.2 eV, and 1.9 eV. The results of normalizing the intensity of these radiation bands to the intensity of the luminescence band in the energy range of 1.9 eV are shown in Table. The choice of the 1.9 eV luminescence band intensity, as the normalizing coefficient is due to the similarity of the excitation mechanisms and the nature of the luminescence centers, as shown in (Baraban, Samarin et al. 2019).

The most significant difference in relative intensity was observed for the band with a maximum energy of 2.2 eV. Note that this EL band is characterized by the maximum excitation energy in the EL

 https://www.doi.org/10.33910/2687-153X-2021-2-1-9-14

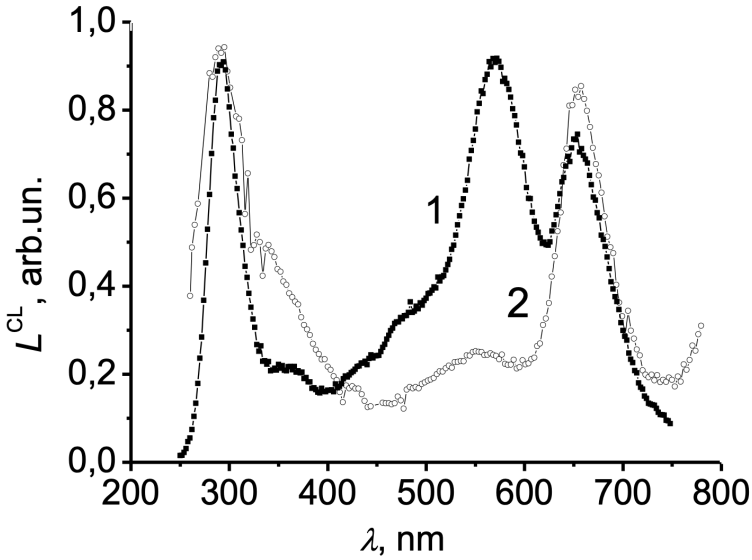

Fig. 1. Luminescence Spectra of a SiO_2 (184 nm) on silicon obtained by CL (1) and EL (2) methods

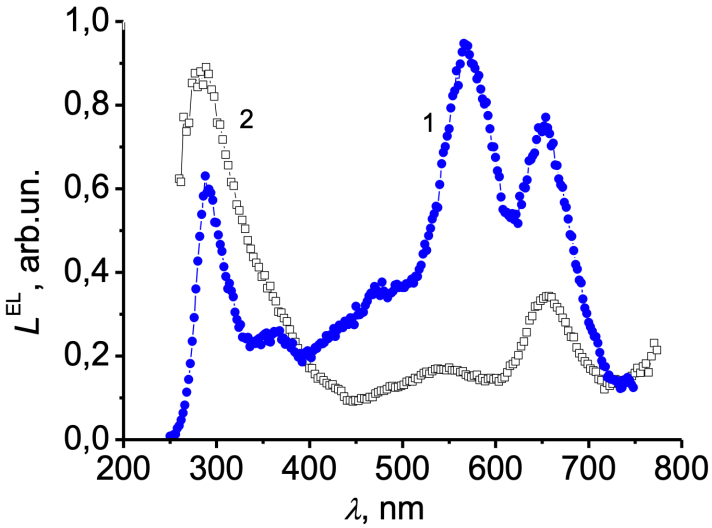

Fig. 2. Luminescence Spectra of a SiO_2 (70 nm) on silicon obtained by CL (1) and EL (2) methods

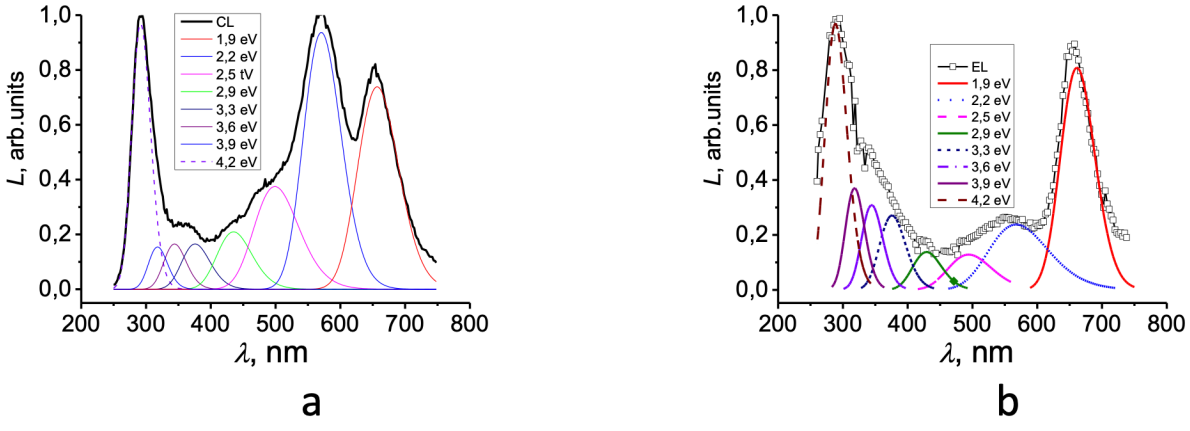

Fig. 3. An example approximation of the CL (a) and EL (b) spectra of Si–SiO_2 structures with an oxide layer thickness of 184 nm by a set of Gaussian distributions

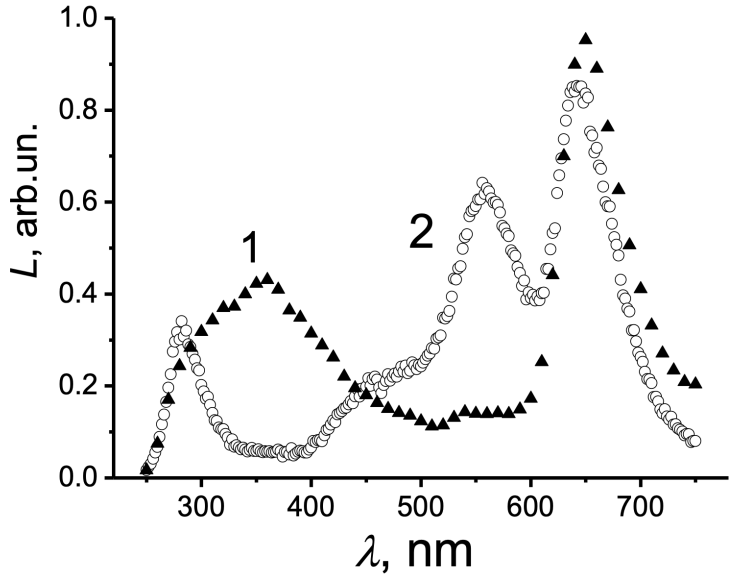

Fig. 4. EL (1) and CL (2) Spectra of SiO_2 layers (100 nm) obtained by thermal oxidation of silicon in a mixture of oxygen and chlorine (Baraban et al. 2012)

Table. Parameters of characteristic CL and EL bands for SiO_2 layers (184 nm). The intensity of spectral bands is indicated in units of the luminescence band intensity of 1.9 eV.

Excitation method	CL	EL
Spectral band, eV	Relative intensity	Relative intensity
1.87 ± 0.04	1	1
2.20 ± 0.05	1.4 ± 0.2	0.2 ± 0.2
4.20 ± 0.1	1.4 ± 0.2	1.1 ± 0.2

spectrum, which is recorded at an electric field strength that does not cause the development of the impact ionization process in the oxide layer (Baraban et al. 2009).The significantly lower intensity of this band in the EL spectra is due to the peculiarities of the excitation a significantly smaller number of hot electrons providing its excitation in comparison with the CL spectrum and even with the EL band with a maximum at 4.2 eV (peculiarities of EL excitation) and, as noted above, a smaller regionexcitation of luminescence centers in comparison with CL (Baraban et al. 2009). There is practically no information in the literature on the mechanisms of excitation, emission, and the nature of this luminescence centers. Therefore, obtaining additional information on the properties of this LC is, undoubtedly, of interest.

To obtain additional information on the properties of LC in the oxide layer, a set of EL and CL spectra was obtained for Si–SiO_2 structures with different oxide layer thicknesses (30–200 nm) and their approximation was carried out using the obtained set of Gaussian distributions. As a result, the dependences of the intensity of the luminescence bands on the thickness of the oxide layer were obtained. It was found that the intensity of the 2.2 eV EL band is proportional to the length of the region of its excitation (d_{ox}-d_0, where $d_0 \approx 30$ nm is the outer part of the oxide layer with no hot electrons). In the case of CL the intensity of the 2.2 eV band is proportional to the energy losses of the electron beam at this thickness of the oxide layer, calculated using the program "Casino" (Drouin et al. 2006). This made it possible to conclude that there is a uniform distribution of LC responsible for the luminescence band with a maximum at an energy of 2.2 eV over the entire thickness of the oxide layer in the thickness range of 30–200 nm. In this case, it is logical to assume that the formation of these LC is a consequence of the thermal oxidation of silicon and is associated with the formation of an equilibrium concentration of oxygen vacancies over the entire thickness of the oxide layer.

 https://www.doi.org/10.33910/2687-153X-2021-2-1-9-14

In the case of a luminescence band with a maximum at anenergy of 4.2 eV, the relative intensity of which is comparable to the EL and CL spectra of Si-SiO_2structures, the dependences of the intensity on the thickness of the oxide layer differ significantly. In the case of EL, the intensity of this band is proportional to the region of its excitation, and in the case of CL, the intensity of the band increases with an increase in the thickness of the oxide layer much more than is assumed for a uniform CL distribution. The final conclusion about the spatial distribution of LC data requires additional studies and detailed analysis.

Luminescence of Ta_2O_5 layer excited by electrons (CL and EL)

Fig. 5 shows the EL and the CL spectrum of Si–Ta_2O_5 structures with a dielectric film thickness of 100 nm. As is seen, the spectrum contains the most efficient band peaking at about 560 nm and a broad short-wavelength wing, which suggests the presence of several overlapping bands. Aggregate analysis of the obtained spectra allowed us to approximate them by a set of Gaussian bands peaking at (*2*) 2.20 eV (564 nm), (*3*) 2.60 eV (477 nm), (*4*) 3.00 eV (413 nm), (*5*) 3.30 eV(376 nm), and (*6*) 3.80 eV (326 nm). The error of determination of peak positions was 0.05 eV.

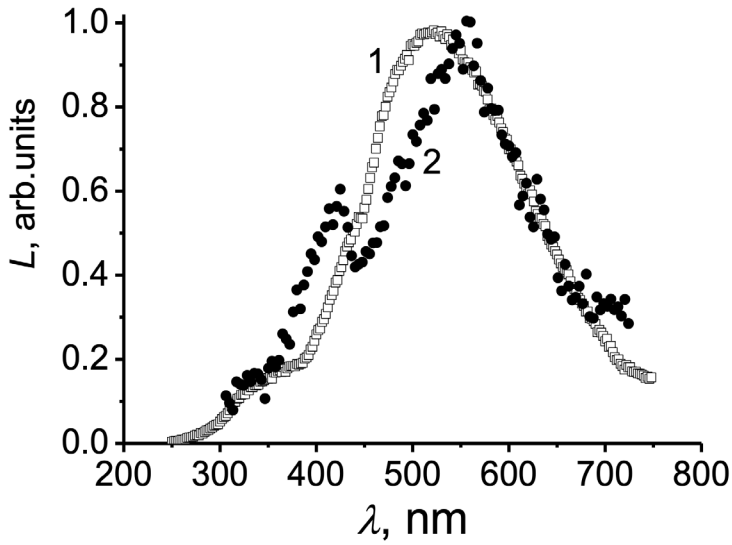

Fig. 5. CL (1) and EL (2) spectrum of Si–Ta2O5 (100 nm) structures

The analysis of approximation results showed a significant decrease in the intensity of the luminescence band with a maximum at an energy of 2.6 eV in the EL spectra in comparison with the CL spectra. It was noted that a decrease in the thickness of Ta_2O_5 layers led to a decrease in the intensity of this EL band up to its complete quenching at a layer thickness of 35 nm. Relative intensities of the remaining emission bands are comparable in a wide range of Ta_2O_5 layer thicknesses. This circumstance, taking into account the specific features of CL and EL excitation of Ta_2O_5 layers, may be used to obtain additional information both on the mechanism of the observed luminescence and the electronic structure of the luminescence center.

To explain this feature, it is necessary to recall that earlier PL studies of Ta_2O_5 layers on silicon (Baraban et al. 2016) showed the presence of localized energy levels in the Ta_2O_5 band gap, which are inherent in luminescence centers. The PL was excited due to the band-band generation of electron-hole pairs and/or the transfer of an electron from the valence band of Ta_2O_5 to the LC energy level in the forbidden band. The minimum EL band intensity of 2.6 eV is due to the fact that the position of this level in the Ta_2O_5 band gap is the most convenient one for the implementation of the hopping conduction of holes from the valence band of silicon to the electrolytic field of the electrode used for recording EL spectra. In this case, the nonradiative channel of electron energy dissipation turns out to be dominant, which manifests itself in the quenching of this luminescence band. In the case of recording CL spectra, the process of charge carrier transfer over localized electronic states in the Ta_2O_5 band gap is absent, which manifests itself in the generation of radiation in the corresponding band. This fact confirms the validity of the previously proposed model and indicates the possibility of its use for electron-excited luminescence in Ta_2O_5 layers.

In addition, the complete resemblance of the form of the CL and EL spectra of Si–Ta_2O_5 structures in the rest of the spectral range indicates the possibility of using the EL method to study the recombination mechanism of luminescence.

Thus, we can conclude that the presence of defects (luminescence centers) in the oxide layer leads to the formation of a set of energy levels in the band gap of Ta_2O_5 layers obtained by ALD, which appear in the luminescence spectra regardless of the excitation method. Note that it is not possible to associate the luminescence centers with the presence of defects caused by oxygen deficiency in Ta_2O_5 layers, since annealing of the structures at 200 °C in an oxygen atmosphere led to an increase in the intensity of the EL and CL spectra, retaining the shape of the spectral distribution.

Conclusion

Based on the approximation of the EL and CL spectra of SiO_2 layers on silicon with a single set of Gaussian emission bands, the dependences of the band intensity on the SiO_2 layer thickness were obtained. On this basis, for the emission band with a maximum at an energy of 2.2 eV, it was concluded that the corresponding luminescence centers are uniformly distributed in SiO_2 layers. It is assumed that the formation of these CL is a consequence of thermal oxidation of silicon and is associated with the formation of the equilibrium concentration of oxygen vacancies. In the case of Ta_2O_5 layers on silicon, a similar approach revealed a significant decrease in the intensity of the emission band with a maximum of 2.6 eV in the case of the EL method, which confirms the participation of luminescence centers in charge transfer processes in Si–Ta_2O_5 structures.

References

Babaran, A. P., Bulavinov, V. V., Troshikhin, A. G. (1993) Changes in the state of Si-SiO_2 structures studied by the method of field cycling in a system with electrolytic contacts. *Technical Physics Letters*, 19 (9), 577–578. (In English)

Baraban, **A.** P., Denisov, E. A., Dmitriev, V. A. et al. (2020) Features of SiO_2 layers synthesized on silicon by molecular layer deposition. *Semiconductors*, 54 (4), 506–510. https://www.doi.org/10.1134/S106378262004003X (In English)

Baraban, A. P., Dmitriev, V. A., Petrov, Yu. V. (2009) *Elektrolyuminestsentsiya tverdotel'nykh sloistykh struktur na osnove kremniya [Electroluminescence in silicon-based solid-state layered structures].* Saint Petersburg: Saint Petersburg State University Press, 195 p. (In Russian)

Baraban, A. P., Dmitriev, V. A., Petrov, Yu. V., Timofeeva, K. A. (2012) Electron-excited luminescence of SiO_2 layers on silicon. *Physics of the Solid State*, 54 (6), 1149–1152. https://www.doi.org/10.1134/S1063783412060066 (In English)

Baraban, A. P., Dmitriev, V. A., Prokof'ev, V. A. et al. (2016) Photoluminescence of Ta_2O_5 films formed by the molecular layer deposition method. *Technical Physics Letters*, 42 (4), 341–343. https://www.doi.org/10.1134/S1063785016040040 (In English)

Baraban, A. P., Selivanov, A. A., Dmitriev, V. A. et al. (2019) Cathodoluminescence of TiO_2 films formed by molecular layer deposition. *Technical Physics Letters*, 45 (3), 256–258. https://www.doi.org/10.1134/S1063785019030210 (In English)

Baraban, A. P., Samarin, S. N., Prokofiev, V. A. et al. (2019) Luminescence of SiO_2 layers on silicon at various types of excitation. *Journal of Luminescence*, 205, 102–108. https://www.doi.org/10.1016/j.jlumin.2018.09.009 (In English)

Coenen, T., Haegel, N. M. (2017) Cathodoluminescence for the 21st century: Learning more from light. *Applied Physics Reviews*, 4 (3), article 031103. https://www.doi.org/10.1063/1.4985767 (In English)

Drouin, D. (2006) CASINO a powerful simulation tool for cathodoluminescence applications, *Microscopy and Microanalysis*, 12 (S02), 1512–1513. https://www.doi.org/10.1017/S1431927606069686 (In English)

Yacobi, B. G., Holt, D. B. (1990) Cathodoluminescence. In: *Cathodoluminescencemicroscopy of inorganic solids*. Boston: Springer Publ., pp. 55–88. https://www.doi.org/10.1007/978-1-4757-9595-0_4 (In English)

Zamoryanskaya, M. V., Sokolov, V. I. (1998) Structural study of thermal-oxide films on silicon by cathodoluminescence. *Physics of the Solid State*, 40 (11), 1797–1801. https://www.doi.org/10.1134/1.1130659 (In English)

Physics of Semiconductors.
Semiconductor Physics

UDC 536.42+539.19

https://www.doi.org/10.33910/2687-153X-2021-2-1-15-24

Relaxation of the dielectric response in thin films of vanadium dioxide

R. A. Castro Arata✉[1], A. V. Ilinskiy[2], M. E. Pashkevich[3], L. M. Smirnova[1], E. B. Shadrin[2]

[1] Herzen State Pedagogical University of Russia, 48 Moika Emb., Saint Petersburg 191186, Russia
[2] Ioffe Institute, 26 Politekhnicheskaya Str., Saint Petersburg 194021, Russia
[3] Peter the Great St. Petersburg Polytechnic University, 29 Politekhnicheskaya Str., Saint Petersburg 195251, Russia

Authors

Rene Alejandro Castro Arata, ORCID: 0000-0002-1902-5801, e-mail: recastro@mail.ru

Aleksandr V. Ilinskiy

Marina E. Pashkevich, ORCID: 0000-0002-3373-4129

Lydia M. Smirnova

Evgeniy B. Shadrin, ORCID: 0000-0002-1423-2852

For citation: Castro Arata, R. A., Ilinskiy, A. V., Pashkevich, M. E. et al. (2021) Relaxation of the dielectric response in thin films of vanadium dioxide. *Physics of Complex Systems*, 2 (1), 15–24. https://www.doi.org/10.33910/2687-153X-2021-2-1-15-24

Received 11 January 2021; reviewed 18 January 2021; accepted 18 January 2021.

Funding: The reported study was funded by RFBR, project number 20-07-00730.

Abstract. The results of studying the processes of dielectric relaxation in thin nanocrystalline films of vanadium dioxide are presented. The existence of a non-Debye relaxation process was revealed, which is due to the presence of a distribution of relaxators over relaxation times according to the Cole-Davidson model. The activation energy of the dielectric relaxation process was found to be E_p = (0.9 ± 0.1) eV. The observed regularities are explained by a model which views the system as a set of relaxators whose physical parameters have different numerical values due to the Gaussian size distribution of nanocrystallites of the VO_2 film. The temperature change in the parameters of the dielectric relaxation process, detected at T = 340 K, indicates that a complex Mott-Peierls semiconductor-metal phase transition occurs at a given temperature in the VO_2 nanocrystalline film.

Keywords: dielectric response, thin films, vanadium dioxide, distribution of relaxators, relaxation time distribution function.

Introduction

Vanadium dioxide (VO_2) occupies a special place among metal oxides, since vanadium is an element with an unfinished *d*-shell, and therefore it is characterized by the presence of strong correlation effects (Ilinskii et al. 2012). Relaxation processes in systems of this kind have a number of unusual properties, the physical nature of which is unclear. This ensures that interest in fundamental research on this material remains. In addition, thin-film oxidized VO_2-based structures are widely used in electronics and optoelectronics (Oleinik 2004). The operation of such devices as thermal relays, light flux restrictors and ultrafast systems for processing optical information is based on the semiconductor-metal phase transition, which occurs in nanocrystalline layers at a critical temperature T_c, providing a record-breaking short (femtosecond) response to external electromagnetic influence. The high sensitivity of nanocrystalline vanadium dioxide layers to external influences makes it convenient to control the temperature of the semiconductor-metal phase transition in a wide range of variation in the numerical values of its parameters and opens up the possibility of creating new generation optoelectronic systems based on VO_2.

In connection with the relevance of the search for solutions to the problems described above, the goal of this work was to use dielectric spectroscopy to reveal the features of dielectric relaxation processes

in thin nanocrystalline vanadium dioxide layers and their relationship with the processes occurring in VO_2 nanocrystallites in the region of semiconductor-metal phase transition.

The advantage of the dielectric spectroscopy method is that this method allows one to monitor directly the change in the dielectric properties of a material in wide frequency and temperature ranges. The analysis of dielectric spectra makes it possible to reveal the dielectric and thermodynamic parameters of VO_2 nanocrystalline layers—such as the frequency spectra of the permittivity ε, relaxation times τ, the tangent of dielectric loss angle tgδ, the value of the activation energy E_a, and many other parameters that are inaccessible to study by other research methods (Castro et al. 2017; Zyryanova et al. 2017). The advantage of dielectric spectroscopy is, in addition, its high sensitivity to changes in the state of extremely thin nanocrystalline films (less than 100 nm thick) of strongly correlated materials, which opens up the possibility of high-precision express control of their electrophysical parameters.

Dielectric spectroscopy is a research method which easily provides reliable information on the parameters of the investigated dielectric thin-film materials in those frequently encountered situations when relaxation processes are not associated with the presence of one relaxation time, but rather with a set of relaxation times varying over a wide range. In such cases, dielectric spectroscopy solves the problem of constructing a function by distributing the relaxation times over their numerical values.

The relaxation time distribution function is the time dependence of the differential distribution function of the "time" density of relaxators dN/dτ—that is, the number of relaxators per unit time interval. The integral of this function with an infinite upper limit is equal to the total number of relaxators. The integral of this function with a variable upper limit is equal by definition to the integral distribution function of the number of relaxators over relaxation times. The presence of such a distribution may be due to the manifestation of physical processes of different nature in the process of relaxation screening of the external electric field.

In the case of dominance of purely electronic processes, it turns out that, following the application of an external electric field, it takes some time to establish a stationary distribution of internal fields and form a stationary concentration of free electrons in the space charge region. The two-parameter empirical Havriliak-Negami (HN) function can be used to obtain a general mathematical description of relaxation processes in thin films of strongly correlated materials (in particular, VO_2) and experimental dielectric spectra of such films (Schönhals, Kremer 2012). This makes it possible to establish the position (τ_0) of the maxima on the time scale and determine the parameters α and β of the HN function for relaxation processes described by formula:

$$\varepsilon^*(\omega) = \varepsilon_\infty + \frac{\Delta\varepsilon}{\left[1 + (i\omega\tau)^{\alpha_{HN}}\right]^{\beta_{HN}}}, \quad (1a)$$

where ε_∞ is the high-frequency limit of the real part of the permittivity, $\Delta\varepsilon$ is the dielectric increment (the difference between the low-frequency and high-frequency limits), $\omega = 2\pi f$, and α and β are the shape parameters describing, respectively, symmetric ($\beta = 1$, $0 < \alpha < 1$) Cole-Cole distribution and asymmetric ($0 < \beta < 1$, $0 < \alpha < 1$) distribution of relaxators according to their times.

The procedure for obtaining an analytical expression for the function *G(τ)* of the temporal distribution of relaxators over their times is reduced to solving the corresponding inverse problem, in which the expression for the function G(τ) is postulated in a simple form using several "free" parameters that are found from the relation (2):

$$\varepsilon^*(\omega) = \varepsilon_\infty + (\varepsilon_s - \varepsilon_\infty)\int_0^\infty \frac{G(\tau)}{1 + i\omega\tau}\, d\tau, \quad (2)$$

where ε_s is the dielectric constant at extremely low frequencies, and τ is the integration parameter.

In this ideology, for the case of simple Debye relaxation with one single relaxator ($\tau = \tau_0$), the function G(τ) is a delta function. For a more complex relaxation, it is necessary to introduce free parameters into the function G(τ), which for the function G(τ) with parameters α, β, and τ_0 lead to an analytical expression for the simplest distribution function G(τ) of the form (Havriliak, Negami 1967):

 https://www.doi.org/10.33910/2687-153X-2021-2-1-15-24

$$G(\tau) = \frac{\left(\frac{\tau}{\tau_0}\right)^{\beta\alpha} \sin(\beta\Theta)}{\pi\tau\left(\left(\frac{\tau}{\tau_0}\right)^{2\alpha} + 2\left(\frac{\tau}{\tau_0}\right)^{\alpha} \cos(\pi\alpha) + 1\right)^{\beta/2}}, \quad (3)$$

where

$$\Theta = \arctan\left(\frac{\sin(\pi\alpha)}{\left(\frac{\tau}{\tau_0}\right)^{\alpha} + \cos(\pi\alpha)}\right) \quad (4)$$

and $0 \leq \Theta \leq \pi$.

In this article, we only use the function G(τ) in its simplest form.

Experimental procedure

Thin-film structures based on vanadium dioxide nanocrystals were obtained by laser ablation by bombarding a V target with radiation from a pulsed neodymium-doped yttrium aluminum garnet IR laser. The radiation power density was 10^7–10^9 W/cm^2, and the radiation pulse duration was 20 ns. The temperature of the substrate during the synthesis was maintained in the range of 400–650°C. The oxygen pressure in the chamber varied within the range from 10^{-2} to $2 \cdot 10^{-1}$ mm Hg. This made it possible to synthesize nanocrystalline layers of vanadium dioxide with nanocrystallites of different sizes. The morphology of the VO_2 film was controlled by analyzing the atomic force images of the film (Il'inskii et al. 2018). The surface area of the film samples was 10×10 mm^2, the thickness of the films was 900 Å, and the resistivity was 7×10^6 Ohm^{-1} m^{-1} at room temperature. The resulting VO_2 films consist of one layer of adjacent columnar nanocrystallites which are in contact with each other by their lateral faces (Fig. 1). Fig. 1 shows a side cut of a monolayer of VO_2 crystallites in the form of a step obtained by the etching method.

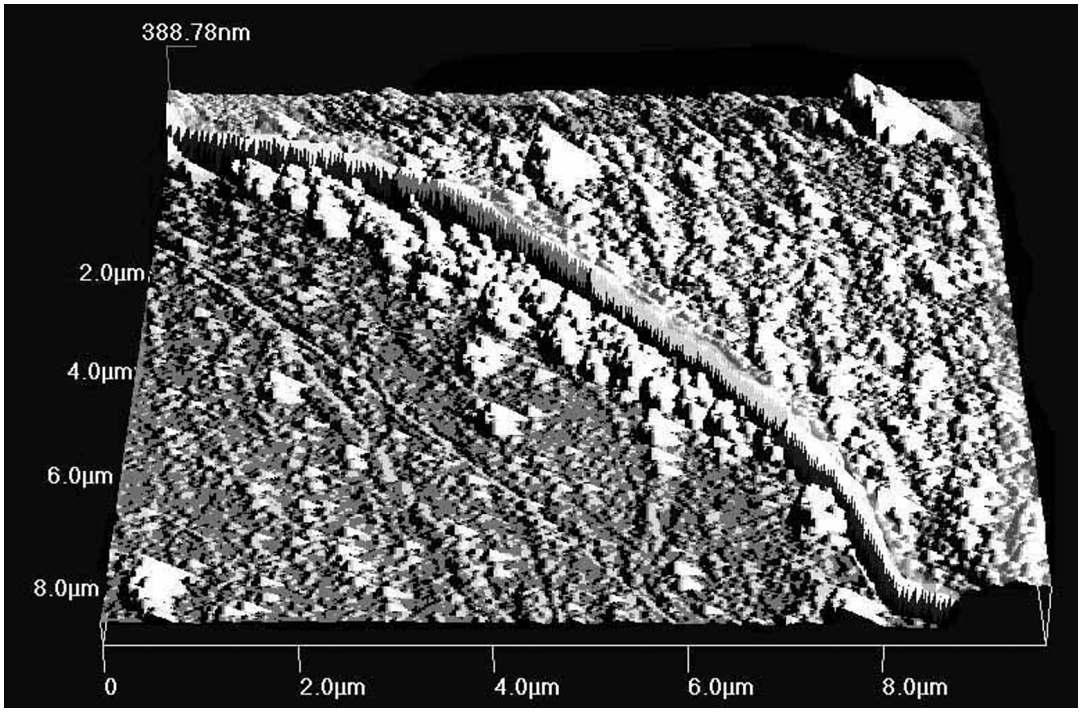

Fig. 1. Atomic-force image of the film surface and its end, obtained by local etching of the film

The measurements of the dielectric spectra of the layers under study were carried out on a Concept-81 spectrometer (Novocontrol Technologies GmbH) designed to study the dielectric and electrical conductivity properties of a wide class of materials. The measurements were carried out in the frequency range $f = 10^2$ Hz…10^6 Hz and temperatures T = 273 K…373 K.

The complex permittivity spectra were calculated from the impedance spectra using the following formulas:

$$\varepsilon^* = \varepsilon' - i\varepsilon'' = \frac{-i}{\omega Z^*(\omega)} \frac{1}{C_0}, \quad (5)$$

where $C_0 = \frac{\varepsilon_0 S}{d}$ is empty cell capacity.

Experimental results

The frequency dependence of the real part of the permittivity ε' at different temperatures for vanadium dioxide films is shown in Fig. 2. The figure shows that ε' decreases with increasing frequency, taking values from 13.7 to 11.6 for a temperature of 273 K. With an increase in temperature, this decrease persists, and the point of the maximum slope of the drop shifts towards high frequencies. For temperatures above T = 340 K, no drop is observed in the frequency range accessible for registration.

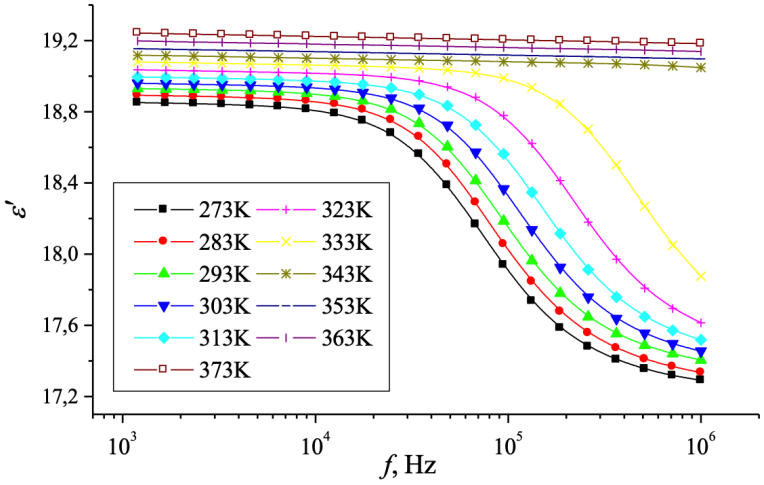

Fig. 2. Frequency dependence of the permittivity ε' at different temperatures

Fig. 3 shows the temperature dependence of the permittivity ε' for a frequency of 10^6 Hz, which follows from the data in Fig. 2. The figure shows that ε' increases with increasing temperature, experiencing a jump in the temperature range T = 340 K.

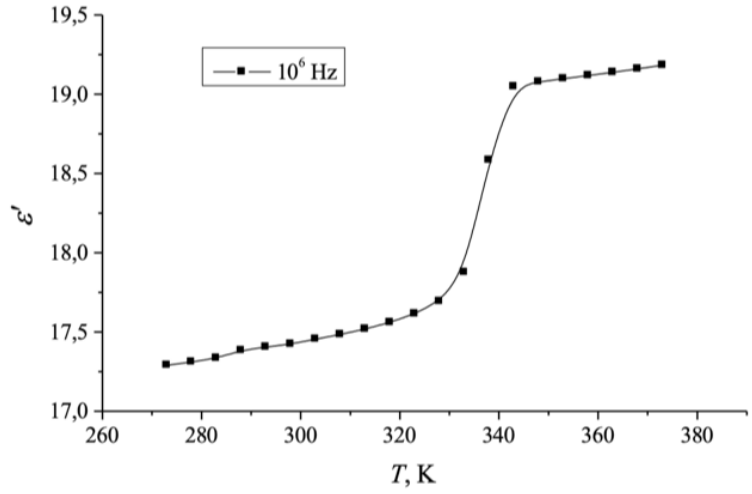

Fig. 3. Temperature dependence of the permittivity ε' of thin nanocrystalline vanadium dioxide layers

https://www.doi.org/10.33910/2687-153X-2021-2-1-15-24

Fig. 4 demonstrates that with increasing temperature, the maximum of the frequency dependence of ε'' shifts towards higher frequencies.

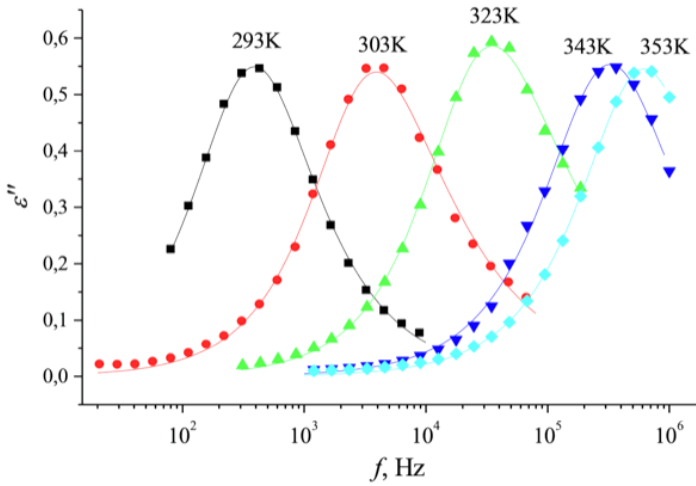

Fig. 4. Frequency dependence of the loss factor ε'' at different temperatures

From the data shown in Fig. 3 and Fig. 4, the frequency dependence of the dielectric loss tangent can be obtained according to the expression $tg(\delta) = \varepsilon''/\varepsilon'$—this expression is not shown, since it behaves similarly to ε'' with changes in frequency and temperature.

Fig. 5 for T = 303 K shows the Cole-Cole diagram (dependence ε'' (ε')) which has the form of a slightly deformed semicircle—this form is due to the asymmetric distribution of the density of relaxators over the relaxation times. Note that at other temperatures in the range of 273–373 K the shape of the diagram remains practically unchanged, and, therefore, no diagrams for other temperatures are shown in Fig. 5.

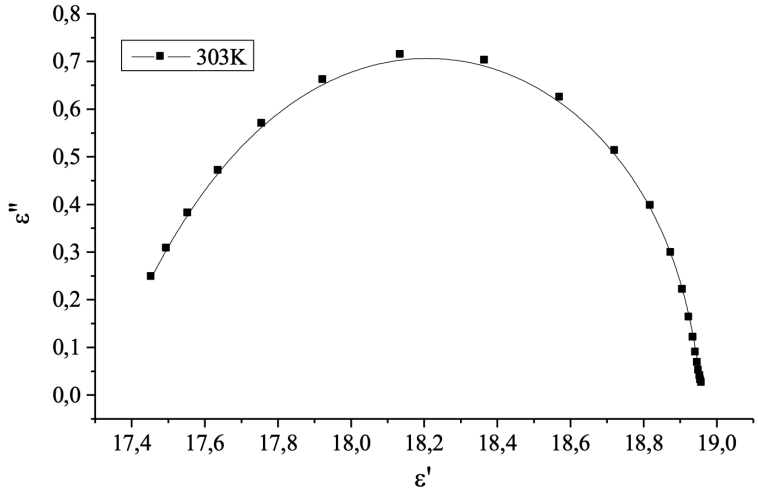

Fig. 5. Cole-Cole diagram of VO_2 layers at temperature T = 293 K (at temperatures T = 323 K, T = 343 K and T = 353 K, the shape of the diagram remains practically unchanged)

The form of the relaxation time distribution function for vanadium dioxide layers is shown in Figs. 6–7 for a set of temperatures: 293, 323, 343 and 353 K. We point out that the integral of this function within the limits (0–∞) is equal to the total number of relaxators. The integral of this function with a variable upper limit is equal by definition to the integral distribution function of the number of relaxators over relaxation times. Fig. 7 shows that at high temperatures $T > T_c$—i.e., at T = 353 K — this function has a symmetrical form. At T = 343 K (that is, near the semiconductor-metal phase transition)

the function exhibits a slight asymmetry. At low temperatures, far from the semiconductor-metal phase transition, the time distribution functions are sharply asymmetric (Fig. 6). In addition, Figs. 6–7 show that, as the temperature rises, the area given by the integral of the above function increases, and it is especially strong in the temperature range of the semiconductor-metal phase transition—that is, the total number of relaxators grows.

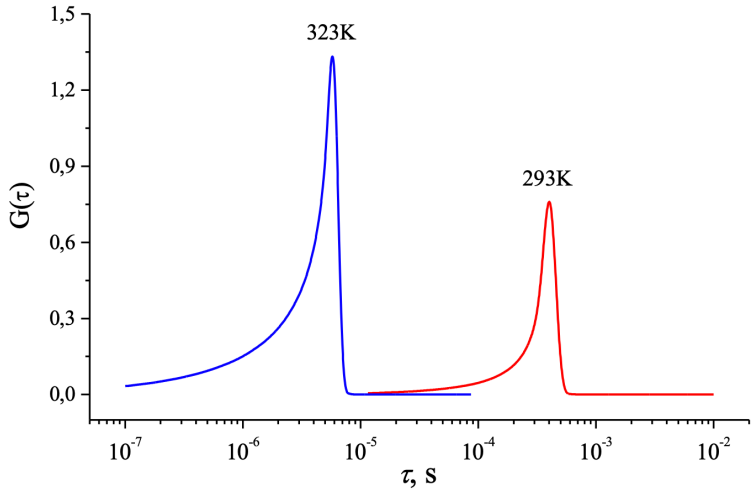

Fig. 6. Form of the distribution function of relaxation times for vanadium dioxide layers at low temperatures up to semiconductor-metal phase transition. The width of the peak of the distribution function at T = 293 K is $\Delta\tau = 2 \cdot 10^{-4}$ s ($\alpha = 0.99 \pm 0.03$; $\beta = 0.88 \pm 0.03$), at T = 323 K it is $3 \cdot 10^{-6}$ s ($\alpha = 0.98 \pm 0.03$; $\beta = 0.62 \pm 0.03$)

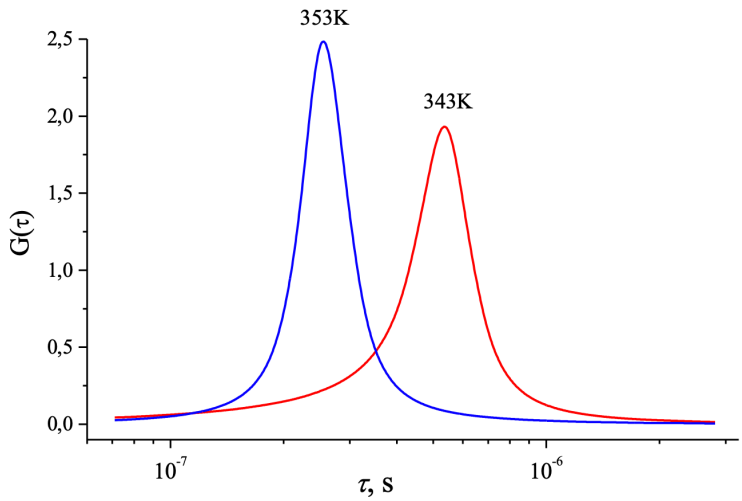

Fig. 7. Form of the distribution function of relaxation times for vanadium dioxide layers at high temperatures after the phase transition. The width of the peak of the distribution function at T = 353 K is $\Delta\tau = 2 \cdot 10^{-7}$ s ($\alpha = 0.96 \pm 0.03$; $\beta = 1.00$), at T = 343 K it is $4 \cdot 10^{-7}$ s ($\alpha = 0.98 \pm 0.03$; $\beta = 0.87 \pm 0.03$)

The temperature dependence of the frequency at which the maximum loss $\varepsilon''_m(\tau_0)$ is observed makes it possible to determine the activation energy of relaxation processes—i.e., the energy barrier required to excite relaxators. The activation energy calculated in Arrhenius coordinates from the slope of the temperature dependence of the most probable relaxation time turned out to be $E_a = (0.9 \pm 0.1)$ eV (Fig. 8).

The discussion of the results

Fig. 2 shows that the real part of the dielectric permittivity has decreased from the value ε_s (13.6) by the value $\Delta\varepsilon$ (13.6 – 11.7 = 1.9) in accordance with formula (2). The monotonic behavior of the frequency dependence $\varepsilon(f)$ is determined by the function $G(\tau)$—that is, by the presence of certain type of relaxators. We believe that the nature of the relaxators is determined by the charge-discharge processes

 https://www.doi.org/10.33910/2687-153X-2021-2-1-15-24

of the capacitances C_i of the film elements and the corresponding sections C_{is} of the substrate, charged through the resistances R_i, which are the resistances of the nanocrystallites of the film at a given temperature. The corresponding equivalent circuit contains C_i and R_i connected in parallel, to which C_{is} is connected in series. In this case, R_i, as well as the conductivity of film nanocrystallites, depend on the temperature T (Ilinskii et al. 2020), while the capacitance values do not depend on T.

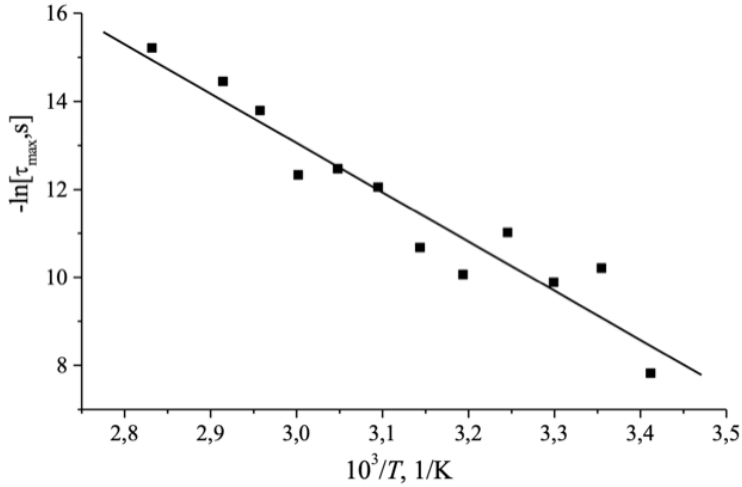

Fig. 8. Temperature dependence of the most probable relaxation time in thin VO_2 layers

The shape of the decay of the function ε(f) is well described by formula (2), in which the function G(τ) is a function of the parameters of one type of relaxators with a characteristic distribution of their "time" density over relaxation times. Of course, the presence of one type of relaxators does not mean that there is one single relaxator (in this case, we would have the function G(τ) in the form of δ-function). We are talking about the presence of relaxators of the same nature with a certain distribution of their relaxation times. That is, the Debye approximation, characterized by a relaxator with a single frequency, is not realized in this case. This conclusion is also confirmed by the shape of the Cole-Cole diagram $\varepsilon''(\varepsilon')$: the presence of one semicircle indicates relaxators of the same nature, and its asymmetry indicates that the Debye approximation is not realized. The form of this function for temperatures of 293–313 K is shown in Fig. 6.

The values of properties exhibited by this type of relaxers are widely dispersed, which is, in our opinion, caused by the similarly wide dispersion of the sizes and size-related electrophysical properties of nanocrystallites (Ilinskii, Castro, Pashkevich et al. 2020).

Figs. 2 and 6–7 show that changes in the characteristic features of the function ε' and the value τ_0 are shifted towards high frequencies up to 10^7 Hz (short times). We associate such a shift with a thermal drop in the resistance R_i of nanocrystallites and, accordingly, a decrease in τ_0 from $3 \cdot 10^{-4}$ s for T = 293 K to $5 \cdot 10^{-7}$ s for T = 343 K. This is confirmed by the behavior of the frequency dependence of the loss factor ε" at different temperatures (Fig. 3). Since the concentration of free electrons increases, and the resistance of nanocrystallites decreases, with increasing temperature, the maximum of dielectric losses ε'' shifts to the high-frequency region. The tangent of the dielectric loss angle $tg(\delta) = \varepsilon''/\varepsilon'$ behaves in a similar way. The monotonic shift of the position of the $tg\delta$ maximum toward high frequencies with increasing temperature up to 335 K also indicates a monotonic decrease in the electrical resistance caused by a thermal increase in the concentration of free electrons in the conduction band. We point out that at T = 340 K there is a sharp increase in the frequency at which the maximum $tg\delta$ (f) is located. We attribute this increase to the completion at this temperature of the semiconductor-metal phase transition at Tc = 340 K. Continuous metallization of nanocrystallites at $T > T_c$ forces one to switch to a fundamentally different equivalent electrical scheme describing relaxation processes. In this case, in the equivalent circuit of the sample, only the capacity of the substrate remains, which we consider to be practically ideal and which is charged with electrons through the mass of film nanocrystallites metallized at $T > T_c$.

The asymmetry of the peaks (Figs. 6, 7) is associated, in our opinion, primarily with the size distribution of nanocrystallites in the film, which at each temperature gives the distribution of nanocrystallites

over the concentration of free electrons—that is, over the screening times of the external electric field by a gas of free electrons. In addition, interactions between electrons, which are characteristic of the highly correlated VO_2 material, contribute to the asymmetry.

Notably, at high temperatures (T = 353 K—i.e., at $T > T_c$), the relaxation time distribution function G(τ) has a symmetric form, and its half-width is $\Delta\tau = 10^{-7}$ s. If this function is described by the HN function, then for it α = 0.96 and β = 1. In the temperature range near the semiconductor-metal phase transition (T = 343) K, there is some asymmetry G(τ), and its half-width is equal to $3 \cdot 10^{-7}$ s. For this case, α = 0.96 and β = 0.87. However, at low temperatures T = 323 K and T = 293 K ($T < T_c$), this function becomes sharply asymmetric and cannot be described by the generally accepted HN function. The model needs to be complicated. The reasons for this complication, in our opinion, are the martensiticity of the semiconductor-metal phase transition and the large role of correlation effects in the process of completing the Mott part of the semiconductor-metal phase transition (Ilinskii et al. 2012).

Notably, such complicated processes are manifested in the presence of a series of maxima on the temperature dependence of the numerical value of the maximum of the function dN/dτ (Fig. 9). In this case, the maximum at T = 340 K is undoubtedly associated with the Peierls structural PPM, while the other maxima in Fig. 9 are due to the peculiarities of the Mott electronic semiconductor-metal phase transition at $T < T_c = 340$ K.

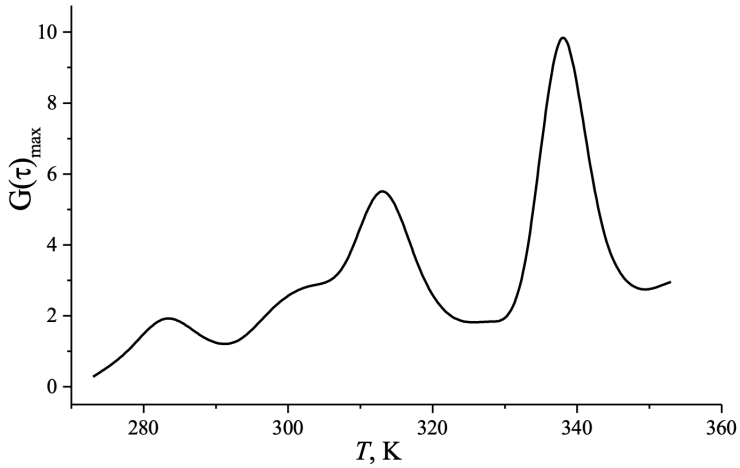

Fig. 9. Temperature dependence of the numerical value at the maximum of the relaxation time distribution function for the studied layers of vanadium dioxide

When describing the detailed reasons for the appearance of certain features in dielectric spectra (in particular, the asymmetry of the HN function) and the appearance of the reasons for such asymmetry, we proceed from the following physical considerations.

1) In the case studied by us, there is one type of relaxators which is realized in vanadium dioxide due to the relaxation process of screening of the external electric field by a gas of strongly correlated free electrons in the conduction band.
2) The parameters of the relaxation process of the dielectric response are significantly affected by the semiconductor-metal phase transition process, which is of a martensitic nature. Namely, the VO_2 film contains nanocrystallites of various sizes distributed according to a law close to a weakly asymmetric Gaussian (Ilinskiy et al. 2020). In this case, the width of the elementary hysteresis loops of individual nanocrystallites is inversely proportional to the square root of their diameter, and the phase equilibrium temperatures (the middle of the elementary loops) for all nanocrystallites are different, being shifted to different degrees towards low temperatures due to differences in the oxygen nonstoichiometry of nanocrystallites. Nonstoichiometry manifests itself in the formation of oxygen vacancies during the synthesis of films which have donor properties. They shift to the low-temperature side the point T_c of thermal equilibrium of the semiconductor and metal phases in a given nanocrystallite—that is, they shift the middle of its elementary loop. The nonstoichiometricity of large grains is much greater than the nonstoichiometry of small grains due to the effective healing of vacancy oxygen defects in small grains. Therefore, even at room temperature, a small part of the largest nanocrystallites turns out to be metallized—that is, at least the Mott part of

 https://www.doi.org/10.33910/2687-153X-2021-2-1-15-24

the VO_2 complex semiconductor-metal phase transition is completed in them into the metallic phase, which is due to the narrowness of their elementary loops.

3) The numerical value of the dielectric relaxation time is inversely proportional to the concentration of electrons in the conduction band. With an increase in the temperature of the semiconductor phase, an increase in the total concentration of free electrons occurs due to an increase in the number of metallized grains that have completed the Mott phase transition.
4) As is known (Ilinskii et al. 2020), the distribution of electrons in energy in such a strongly correlated material as VO_2 obeys the Migdal distribution, the mathematical expression for which contains the correlation energy, along with the Fermi energy, in the exponent. The correlation energy of electron-electron interaction consists of two parts: the energy of interaction of free thermally excited electrons of the conduction band with electrons of the atomic core, and the energy of direct Coulomb interaction of free electrons with each other.

At low temperatures of the semiconductor phase, the concentration of free electrons in individual nanocrystallites is low and strongly differs in nanocrystallites of different sizes, since the degree of their oxygen deficiency is sharply different, as indicated above.

This leads to a difference in the concentrations of free electrons in them and, accordingly, leads to a dispersion of relaxation times in nanocrystallites of different sizes. The long "tail" of the G(τ) function, which extends towards short relaxation times, thus reflects the "tail" of the size distribution of nanocrystallites in the film (Ilinskiy et al. 2020).

As the temperature of a set of nanocrystalites increases, these differences are smoothed out due to an increase in the degree of metallization—that is, an increase in the total concentration of free electrons, and an increase in the role of the direct Coulomb interaction between them (Apinyan, Kopeć 2015).

This manifests itself in a decrease in the numerical values of the relaxation times, and upon the transition to the metallic phase of most of the nanocrystallites of the film (for example, at T = 353 K), and in the complete symmetrization of the G(τ) maximum, since practically all nanocrystallites acquire the same concentration of free electrons and the same energy of direct Coulomb interaction between them. There only remains the fluctuation broadening of the maximum of the function G(τ) of the distribution of relaxation times over their numerical values.

Thus, an increase in the degree of total metallization of the film leads to a shift in the maximum of the G(τ) function of the spectral density distribution of relaxators over relaxation times towards shorter times, the G(τ) function becomes more symmetric, and its area and height increase, which is associated with an increase in the number of relaxators due to the involvement of new nanocrystallites of ever smaller sizes in the metallization process. The process ends at the temperature at which complete metallization of the VO_2 film occurs and the process of thermal growth of the concentration of free electrons saturates.

Conclusion

The work investigates the processes of dielectric relaxation in thin films of vanadium dioxide in the temperature range T = 273–373 K. The frequency dispersion of the dielectric permittivity and the presence of maxima in the spectra of dielectric losses are revealed, which indicates the existence of relaxation processes. The experimentally determined values of the relaxation parameters convincingly demonstrate the existence of a distribution of relaxators over relaxation times. According to the Cole-Cole model for the case of a symmetric distribution of relaxation times at high temperatures (at temperatures above the semiconductor-metal phase transition temperature), $\alpha = 0.96 \pm 0{,}03$ and $\beta = 1{,}00$. According to the Cole-Davidson model for the case of an asymmetric distribution of relaxation times (at $T < T_c$), $\alpha = 0.99 \pm 0{,}03$ and $\beta = 0.62 \pm 0{,}03$. The activation energy of relaxation processes turned out to be $E_a = (0.9 \pm 0.1)$ eV, which coincides with the numerical value of the band gap of vanadium dioxide at room temperature. The change in the nature of the dispersion of the dielectric permittivity, as well as the observed radical change in the numerical value of the G(τ) function at the maximum at T = 340 K, are due to the semiconductor-metal phase transition performed by VO_2 vanadium dioxide at a given temperature.

References

Apinyan, V., Kopeć, T. K. (2015) Probing phase coherence via density of states for strongly correlated excitons. *Journal of Low Temperature Physics*, 178, 295–330. https://www.doi.org/10.1007/s10909-014-1264-8 (In English)

Castro, R. A., Ignatiev, A. I., Nikonorov, N. V. et al. (2017) Dielectric properties of silver-containing photo-thermo-refractive glass in temperature range of – 50 to + 250 °C: The role of hybrid molecular clusters. *Journal of Non-Crystalline Solids*, 461, 72–79. https://www.doi.org/10.1016/j.jnoncrysol.2017.01.041 (In English)

Havriliak, S., Negami, S. (1967) A complex plane representation of dielectric and mechanical relaxation processes in some polymers. *Polymer*, 8, 161–210. https://www.doi.org/10.1016/0032-3861(67)90021-3 (In English)

Ilinskii, A. V., Castro, R. A., Pashkevich, M. Ye., Shadrin, E. B. (2020) Dielectric spectroscopy and features of the mechanism of the semiconductor–metal phase transition in VO_2 films. *Semiconductors*, 54 (2), 205–211. https://www.doi.org/10.1134/S1063782620020116 (In English)

Il'inskii, A. V., Kastro, R. A., Nikulin, E. I., Shadrin, E. B. (2018) Dielectric spectroscopy of strongly correlated electronic states of vanadium dioxide. *Technical Physics*, 63 (6), 851–856. https://www.doi.org/10.1134/S1063784218060129 (In English)

Ilinskii, A. V., Kvashenkina, O. E., Shadrin, E. B. (2012) Phase transition and correlation effects in vanadium dioxide. *Semiconductors*, 46 (4), 422–429. https://www.doi.org/10.1134/S1063782612040094 (In English)

Ilinskiy, A. V., Nikulin, E. I., Shadrin, E. B. (2020) Comparative analysis of semiconductor-metal phase transition mechanisms in vanadium oxides (V_2O_3 and VO_2). *Physics of Complex Systems*, 1 (3), 113–122. https://www.doi.org/10.33910/2687-153X-2020-1-3-113-122 (In English)

Schönhals, A., Kremer, F. (2012) Analysis of dielectric spectra. In: Kremer, F., Schönhals, A. (eds.). *Broadband dielectric spectroscopy*. Berlin; Heidelberg: Springer Publ., pp. 59–98. https://doi.org/10.1007/978-3-642-56120-7_3 (In English)

Oleinik, A. C. (2004) *Plenki dioksida vanadiya v ustrojstvakh indikatornoj tekhniki i mikroelektroniki [Vanadium dioxide films in display equipment and microelectronics]. Extended abstract of the PhD dissertation (Technical Science). Saratov*, Yuri Gagarin State Technical University of Saratov, 34 p. (In Russian)

Zyryanova, K. S., Kastro, R. A., Pshenova, A. S. et al. (2017) Dielectric properties of silver-doped nanoporous silicate glasses in the temperature range between –50 and +250°C. *Glass Physics and Chemistry*, 43 (3), 207–214. https://www.doi.org/10.1134/S1087659617030142 (In English)

Physics of Semiconductors. Polymer Physics

UDC 541.64+539.233+537.31 https://www.doi.org/10.33910/2687-153X-2021-2-1-25-32

Piezo-active composite systems based on porous polyvinylidene fluoride films and conducting polymer layers as electrodes

G. K. Elyashevich✉[1], I. S. Kuryndin[1], E. Yu. Rosova[1], D. I. Gerasimov[2], M. E. Vylegzhanina[1]

[1] Institute of Macromolecular Compounds, Russian Academy of Sciences, 31 Bolshoy Ave., Saint Petersburg 199004, Russia
[2] Saint-Petersburg State Institute of Technology, 26 Moskovskii Ave., Saint Petersburg 190013, Russia

Authors

Galina K. Elyashevich, ORCID: 0000-0002-9019-1028, e-mail: elyashevich@mail.ru

Ivan S. Kuryndin, ORCID: 0000-0003-0613-9460

Elena Yu. Rosova, ORCID: 0000-0002-8608-3024

Dmitrii I. Gerasimov, ORCID: 0000-0001-8126-5630

Milana E. Vylegzhanina, ORCID: 0000-0002-4334-7595

For citation: Elyashevich, G. K., Kuryndin, I. S., Rosova, E. Yu., Gerasimov, D. I., Vylegzhanina, M. E. (2021) Piezo-active composite systems based on porous polyvinylidene fluoride films and conducting polymer layers as electrodes. *Physics of Complex Systems*, 2 (1), 25–32. https://www.doi.org/10.33910/2687-153X-2021-2-1-25-32

Received 8 December 2020; reviewed 16 December 2020; accepted 16 December 2020.

Abstract. The study has obtained composite systems containing porous polyvinylidene fluoride films and electroconducting polymers—polyaniline and polypyrrole. Porous supports were prepared by melt extrusion. It was shown by scanning electron and atomic force microscopy that porous PVDF films have a relief surface, and a higher surface roughness improves hydrophilicity of supports. The layers of conducting polymers on the surface of porous supports were formed by oxidative polymerization in situ in monomer solution. It was found that conducting coatings have high adhesion of conducting layers to the porous films due to the relief surface of the PVDF film. Composites have surface and volume conductivity on the order of 10^{1} S/cm and 10^{-6}–10^{-5} S/cm, respectively. The layers of conducting polymers were used as electrodes to polarize the composites and to measure piezomodulus d_{31}. The maximum value of d_{31} was 18 pC/N.

Keywords: polyvinylidene fluoride, polyaniline, polypyrrole, porous films, electrical conductivity, piezoelectric modulus.

Introduction

Composite systems based on polyvinylidene fluoride (PVDF) and conducting polymers such as polyaniline and polypyrrole draw attention because they combine piezoelectric properties of a PVDF support and high electroactivity of conductive components. Therefore, these materials may find an effective application in energy harvesting, conversion and storage devices. The materials may be used as sensors and transducers in hydroacoustics, as effective membranes in filtration and separation processes as well as as separators in electric batteries (Bar-Cohen, Zhang 2008; Chang et al. 2007; Dang et al. 2013; Lebrun et al. 2009; Salimi, Yousefi 2003). PVDF is one of the promising polymer piezoelectric materials due to its chemical stability and outstanding mechanical characteristics. It also has important advantages over inorganic piezoelectrics such as high processibility, low density, elasticity and environmental safety of production.

Piezoelectric properties of PVDF-based materials are related to the polymorphic character of its crystal phase which contains nonpolar and polar modifications (α, β, γ и δ). Among these modifications the polar β-form has the best piezoelectric characteristics (Branciforti et al. 2007). Research in the

development of PVDF-based piezo elements focuses on increasing the content of piezoactive β-crystallites and deposition of electrode layers on the surface of piezoelectric films. One of the promising ways to improve the transducer parameters is the formation of a porous film structure. It was shown (Gerhard-Multhaupt 2002; Yarysheva et al. 2012) that porous materials demonstrate higher piezo constants in comparison with nonporous electrets.

To use PVDF piezo materials as transducers of mechanical energy to electric energy, it is necessary to deposit contacts (electrodes). Here, the main challenge is to activate the hydrophobic surface of PVDF to ensure adhesion of conducting layers. In addition, electrodes have to meet several requirements: the uniformity of the layer, no direct contact between two layers on the film surfaces, good electroconductivity along the surface and elasticity of the composite. Current methods for depositing electrodes are expensive, ineffective or/and labor-intensive. Traditionally, metallic coatings are used as electrodes. However, the formation of conducting polymer layers is a much more effective technology than vacuum deposition of metals (Dang et al. 2013). Due to electrical, magnetic, optical and oxidation/reduction properties, conducting polymers (polyaniline, polypyrrole, polythiophene, etc.) have a wide application in membranes, electrochemical sensors, pressure transducers and other devices (Liu et al. 2011; Merlini et al. 2014; Ozkorucuklu et al. 2012).

The purpose of the research is the development of effective methods to form electroconducting polymer layers (polyaniline and polypyrrol) as electrodes on the surface of PVDF porous films as supports. It also aims to investigate the structure and surface morphology of the prepared samples, as well as polarization and measurements of piezoelectric modulus for composites.

Experimental methods

PVDF porous films were prepared in five stages: melt extrusion, isometric annealing of extruded films at the temperature close to polymer melting point (170°C), two stages of uniaxial extension— a "cold" stage at room temperature and "hot" stage at 100°C (pore formation stages), and thermal fixation of porous structure at 100°C. Polymer Kynar-720 (Atofina Chemicals Inc., USA), $M_w = 1.9 \times 10^5$, was used for in the preparation process (Elyashevich et al. 2019).

Porous structure of the samples was characterized by the value of overall porosity (P) measured gravimetrically. The value P was calculated as

$$P = [(\rho - \rho_{p)} / \rho] \cdot 100\%,$$

where ρ is the density of a monolithic PVDF film (1.78 g/cm^3) and ρ_p is the density of porous film, determined by weighing.

Composite samples were prepared by the deposition of conducting polymers (polyaniline, polypyrrol) in oxidative polymerization *in situ* directly on the surface of PVDF porous films. The content x of conducting polymer in the prepare d composites was calculated as

$$x = \Delta W_{cond} / (W_{PVDF} + \Delta W_{cond}) \cdot 100\% ,$$

where W_{PVDF} is the mass of initial porous PVDF film and ΔW_{cond} is the mass difference between the composite sample and PVDF support.

Vertex 70 spectrometer (Bruker, USA) recorded Fourier transform infrared (FTIR) spectra.

The surface morphology of samples was studied by scanning electron microscopy (SEM) using SUPRA-55VP tool (ZIESS, Germany) and atomic force microscopy (AFM) using Nanotop NT-206 (Mikrotestmashin, Gomel, Belarus). The measurements were carried out in semi-contact and contact modes under atmospheric conditions using NSC11/AlBS silicon cantilevers with a stiffness coefficient of k = 1.5–5.0 N/m and the radius of curvature of the tip less than 10 nm. The experimental data were processed with the Surface Explorer software.

Wettability of the sample surface was determined by the contact angle technique on DSA30 (KRUSS, Germany).

Electrical conductivity was measured at room temperature by the DC four-probe van der Pauw method using a P-30 potentiostat (Elins, Russia).

PVDF supports were polarized by the contact high voltage DC polarization in the electric field of 80–90 V/μm at temperature of 90°C for 1 h.

 https://www.doi.org/10.33910/2687-153X-2021-2-1-25-32

Piezoelectric modulus d_{31} was determined from static tension applied along the orientation direction of the polarized film. The potential difference arising on the contact electrodes (the conducting polymer layers) during the sample deformation was measured using the P-30 potentiostat.

Results and discussion

Characteristics of PVDF supports

The prepared porous structure of PVDF supports is controlled by orientation parameters at the extrusion stage (melt draw ratio λ) and at the stages of uniaxial extension (degrees of extension ε_1 and ε_2). It was observed (Dmitriev et al. 2017) that crystalline structure of extruded and annealed films is formed by the stacks of lamellar crystals located parallel to each other and perpendicular to the melt orientation direction. The lamellae are connected by the "bridges" of stressed tie chains. Orientation efforts at uniaxial stages lead to the separation of lamellae and the appearance of the voids (pores) between them. When the number and size of pores is growing bigger due to stronger orientation efforts, the through channels are formed in the film. It is the result of a percolation mechanism when the value of overall porosity reaches the percolation threshold (P = 23% for these samples). The obtained porous films vary in porosity and size of pores due to the parameter-controlled preparation process (Table 1).

Table 1. Characteristics of PVDF porous films

Thickness	10–25 microns
Overall porosity	12–30%
Average size of pores	33 nm
Maximal size of pores	60–80 nm
Surface roughness (R_a and R_q)	45–55 nm and 60–90 nm
Specific surface	25–37 m^2/g
Breaking strength	125–145 MPa
Elongation at break	30–50%

The porous films are marked by a strongly developed relief-like surface (Elyashevich et al. 2019). It is the result of stress release to the surface which leads to the development of through pores. It was shown that the scale of relief increases when orientation parameters are higher—λ and ε, i.e. bigger overall porosity provides an increase in height in a particular surface area (S) (Table 1). Note that the value S for these porous films is on the order of several tens of m^2/g, while for nonporous (i.e., initially extruded and annealed) films it is approximately 10^{-4} m^2/g.

To estimate the scale of the surface relief, the porous PVDF films were investigated by AFM method (Fig. 1). Figure 1 shows AFM images of the film prepared at λ = 76, ε_1 = 50% and ε_2 = 40%. In the 3D image (a) and the image of the surface height (b), oriented lamellae with a thickness of ~100–200 nm are clearly visible. By analyzing the profile of the selected surface area (c), it is possible to estimate the pore depth, which reaches a value of 400 nm relative to the ridge of the lamella. The values of the arithmetic mean (R_a) and root-mean-square (R_q) surface roughness for the 30×30 μm scanning matrix are 78.8 nm and 97.9 nm, respectively.

The analysis of AFM pictures of the porous films evidences that roughness of the surface increases along with an increase of orientation parameters and, as a result, it impacts the porosity of the samples. It is known that PVDF is a rather hydrophobic material, it is poorly wetted by water: dense PVDF films have a contact angle (θ) of nearly 75°. If porosity increases from 12 to 30%, the values of θ for the porous films decrease from 71 to 65° (Fig. 2b and 2c), i.e., higher roughness of the surface positively impacts hydrophilicity of the samples. This result is consistent with commonly accepted conception concerning the influence of surface relief on wettability of material (Boinovich, Emelyanenko 2008).

The preparation of composite PVDF/conducting polymers

The PVDF/conducting polymer samples were obtained by *in situ* oxidative polymerization of monomer directly on the surface of a PVDF support. To prepare the PANI/PVDF composites the support was placed into a reaction mixture containing the solution of aniline hydrochloride in 1 M HCl; then the

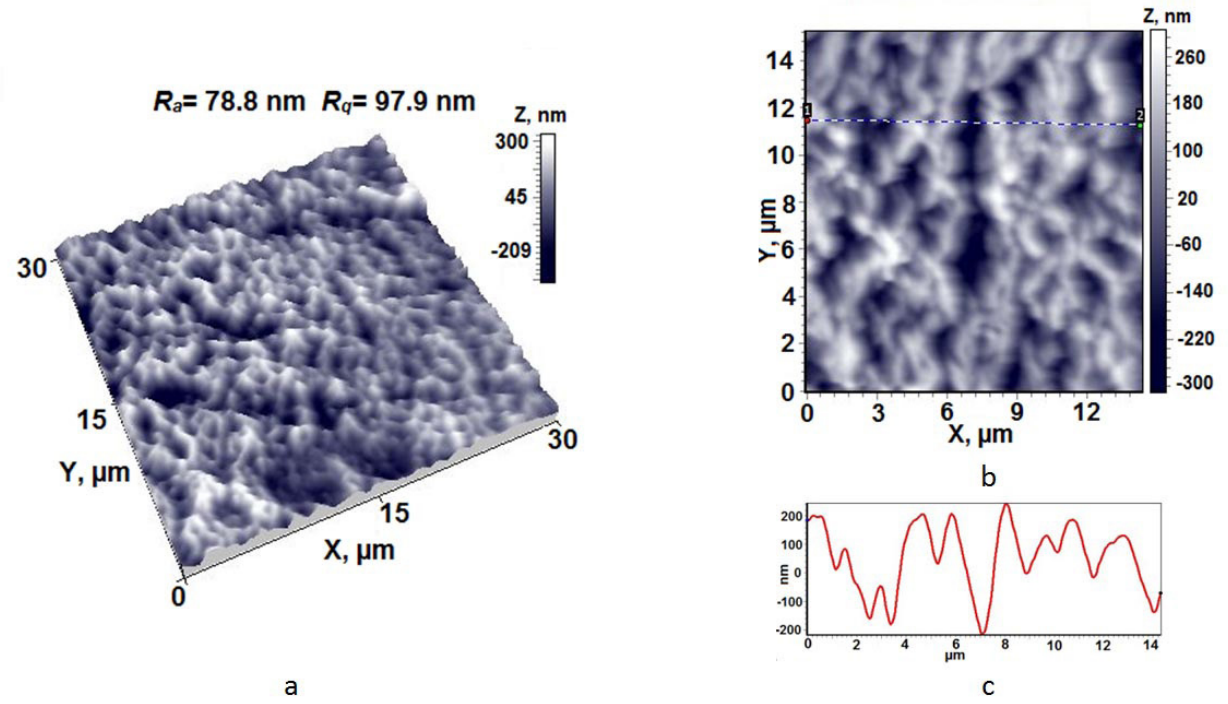

Fig. 1. AFM images of the surface for the porous PVDF film (P = 28%): a—surface topography, b—3D image, c—profile of the selected surface area

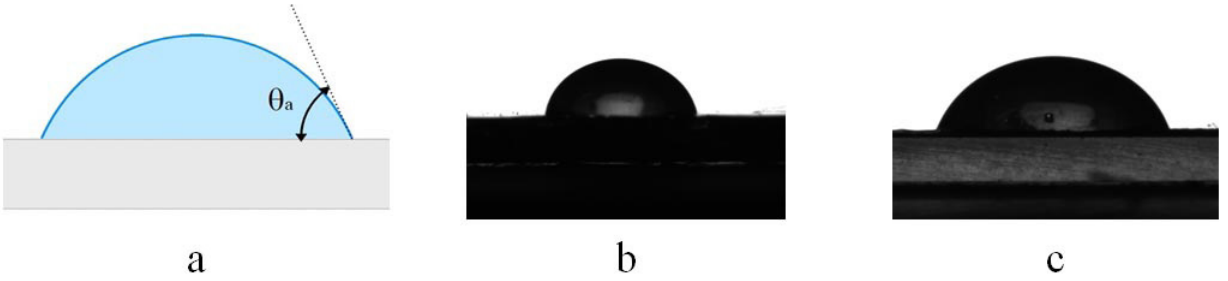

Fig. 2. Wettability by water of PVDF porous films: a—schematic image of a water drop on the film surface and contact angle θ; b—porous film with P = 13%, c—porous film with P = 28%

solution of ammonium persulfate was added as an oxidant. As a result, a PVDF film covered by green polyaniline layer was obtained. We also performed second polymerization of aniline hydrochloride on the surface of the obtained film to increase the content of conducting polymer and to form a PANI layer with higher density and homogeneity. It was carried out by placing the prepared sample in a fresh polymerization mixture.

The layers of polypyrrole (PPy) were formed on the surface of a PVDF support by polymerization of monomer (pyrrole) in the mixed solution of methanol and water in equal volumes. The solution used $FeCl_3$ as an oxidant. The mixture of methanol/water was chosen as an optimal solvent which ensures the best wettability of a PVDF surface and the formation of a homogeneous defect-free PPy layer.

It was observed that the content of conducting polymer in the composite grows along with an increase in overall porosity (Fig. 3). Figure 3 also shows that the dependence becomes stronger at the value of porosity that corresponds to the appearance of through channels (more than 23%). This provides better conditions for the PPy layer formation.

 https://www.doi.org/10.33910/2687-153X-2021-2-1-25-32

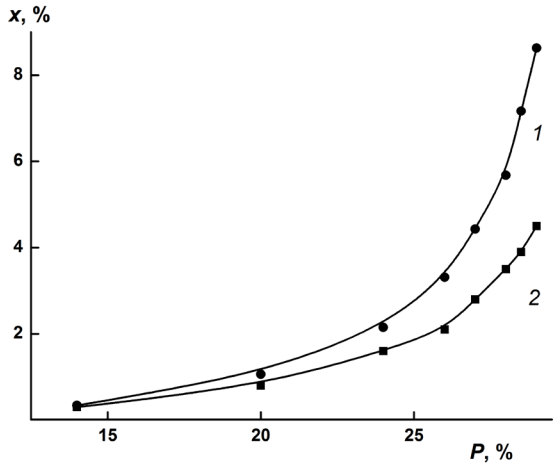

Fig. 3. Content of PPy (1) and PANI (2) in composites vs porosity of a PVDF support

Morphology of composites

Morphology of composite films was studied using scanning electron microscopy. Fig. 4 shows the surfaces of PANI/PVDF and PPy/PVDF composites in comparison with a PVDF support. The SEM picture of the PVDF support demonstrates its developed relief structure: surface comb-like peaks and cavities between them. The SEM image of PVDF/PANI shows that polyaniline fills the pores and forms the so-called cauliflower structure on a PVDF surface. Fig. 3c shows that the surface of a PPy layer has a globular structure typical of PPy, and the conducting coating fully masks the support relief (as is seen in Fig. 3, the content of PPy in the composite is twice higher than the content of PANI).

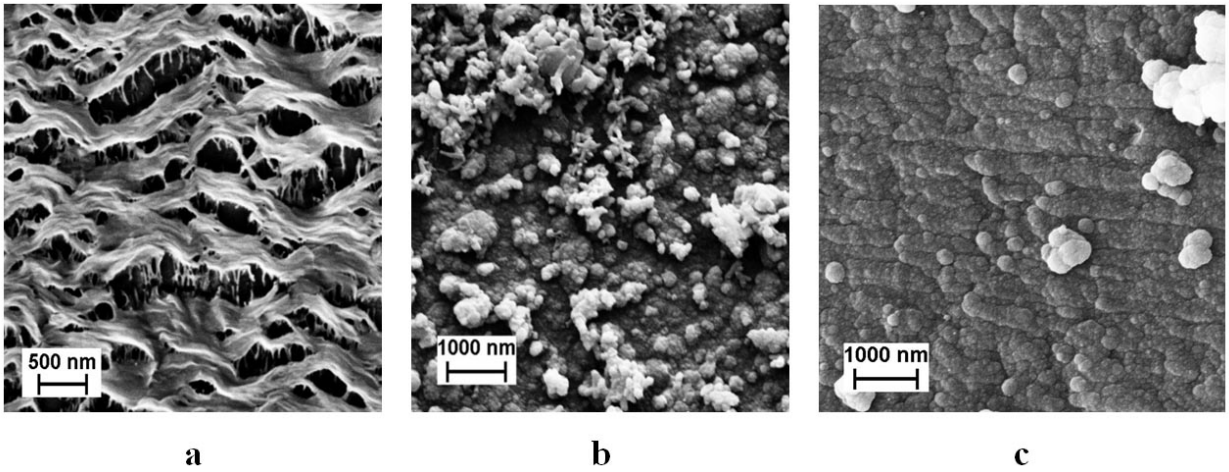

Fig. 4. SEM pictures (surface) of PVDF films (a) and PVDF/PANI (b) and PVDF/PPy (c) composites

It was established that the obtained conducting layers have a high adhesion to the porous PVDF films, and no exfoliation was observed during the mechanical bending of the composites. At the same time, PPy and PANI layers were easily separated from the smooth dense support. It means that relief-like surface and porous structure provide adhesion between the components of the composite samples. This conclusion is confirmed by IR spectroscopy investigations. It is clearly seen (Figs. 5 and 6) that at the spectra of the composites the bands of the initial components are presented without any changes or shifting. It means that there are no chemical interactions between the components and conducting layers adhere to the porous support through the so-called mechanical adhesion. Note that high adhesion of the PVDF films under study is also related to the formation of a conducting polymer layer in deep pores opening to the surface (Elyashevich et al. 2002).

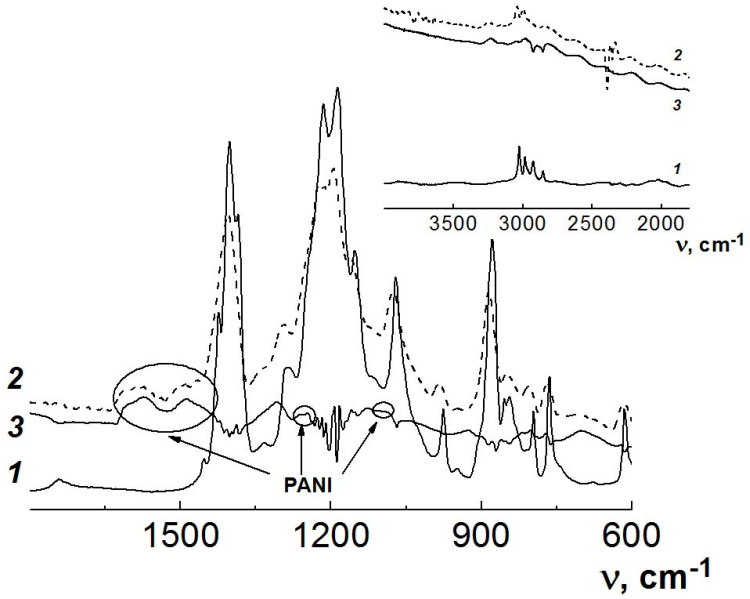

Fig. 5. IR spectra of porous PVDF films (1), PVDF/PANI composites (2), and the resulting difference spectrum (3). Inset: the region of conductivity plateau for PVDF/PANI sample (2) and the difference spectrum (3)

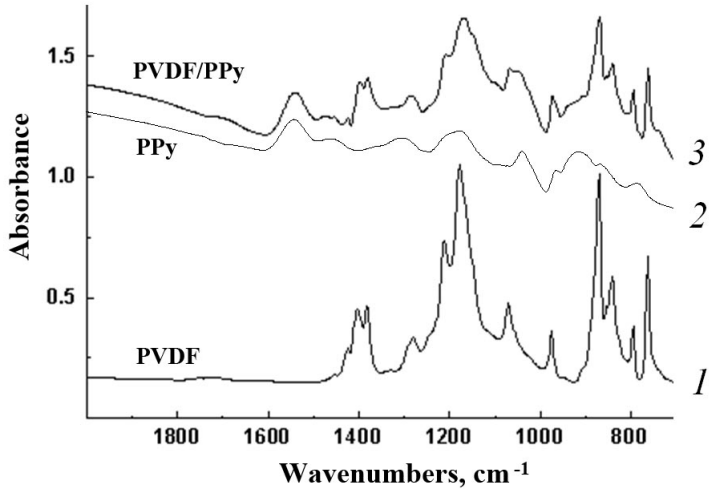

Fig. 6. IR spectra of a PVDF support (1), polypyrrole (2) and PVDF/PPy composites

Fig. 5 shows the IR spectra of a PVDF film, a PVDF/PANI film as well as the spectrum obtained by subtraction of these two spectra. The composite spectrum clearly shows the sample conductivity: absorption bands at 1570 and 1480 cm^{-1} typical for the vibrations of quinoid and benzoid rings that corresponds to protonated (conducting) form of PANI—emeraldine salt. The insert shows the so-called plateau of conductivity where conductive PANI exhibits a weak slope; it is absent in the initial PVDF spectrum. In summary, it is the evidence that PANI is polymerized on the surface of a PVDF porous film to a conductive form.

PANI and PPy are rigid-chain polymers, and their presence in composites often results in their lower mechanical strength and elasticity. However, we did not observe such changes in the prepared composites and they had the same values as the support (Table 1). It is important to note that the composites preserve mechanical integrity during deformation or even a break.

 https://www.doi.org/10.33910/2687-153X-2021-2-1-25-32

Conductivity and piezoelectric properties of PVDF/conducting polymer composites

Electric properties of the composites were characterized by surface and volume conductivity (Table 2). It was observed that conductivity increases along with an increase in the porosity of the support because the content of conducting polymer increases due to a bigger number and sizes of pores (Fig. 3). The volume conductivity is provided by conducting layers which are polymerized on the walls of pores and in the interlamellar regions. The deeper the monomer penetrates in the volume of a PVDF film (penetration depth also depends on wettability of the support by solvent during polymerization and its chemical nature) and the more content of the conducting component it produces, the higher the value of conductivity.

Table 2. Conductivity of the composites PVDF/conducting polymer

Sample	Content of conducting component, %	Surface conductivity, S/cm	Volume conductivity, S/cm
PVDF/PANI	5	3.0	10^{-6}
PVDF/PPy	8	6.0	10^{-5}

The conducting layers of polyaniline and polypyrrole were used as electrodes during polarization to investigate the piezoelectric properties of the prepared PVDF/PANI and PVDF/PPy composites. The piezo effect was characterized by modulus d_{31}. The value of the modulus is determined by the content of the polar piezo-active β-phase in a PVDF crystal structure. Extruded and annealed films contain only non-polar α-form of crystals. During the preparation of porous PVDF films the β-crystals are formed during uniaxial extension as a result of a polymorphous α - β transition. It was shown in (Elyashevich et al. 2019) that the content of β-phase increases at growth of orientation degrees (ε_1 and ε_2) at uniaxial extension stages. At the same time, it was observed that an increase in orientation at the extrusion stage (λ) leads to a decrease in β-form content formed at the subsequent α - β transformation under uniaxial deformation. The effect of negative influence of melt crystallization at high λ was explained by the data of X-ray investigations: α-crystals in the weakly-ordered spherulite structure which is formed at low λ is more effectively transformed into β-phase than more oriented lamellar structure arising at crystallization in higher oriented melt (Gerasimov et al. 2020).

To realize the piezo effect the composites were polarized in a constant electric field. In this work, the samples were polarized by the contact method at an elevated temperature at electric field E_{pol} = 90 V/μm, temperature T_{pol} = 90°C during 1 hour. The measurements of the modulus were carried out under the load of 5–10 MPa in the direction of film orientation. After the polarization all the samples exhibited piezoelectric properties. The highest values of the piezoelectric modulus d_{31} are presented in Table 3.

Table 3. Piezoelectric properties of PVDF/conducting polymers composites

Sample	Overall porosity, %	Content of β phase, %	d_{31}, pC/N
PVDF/PPy	13	60	18
PVDF/PANI	27	43	12

To compare the efficiency of using conducting polymers as an electrode material, the electrodes of liquid indium-gallium alloy were also used. It was found that the value of d_{31} measured by applying polymer electrodes did not differ from the values obtained for the same PVDF films with metallized surfaces. This is the evidence that conducting polymer layers may be effectively used as electrodes.

Conclusion

In our study, composite piezo-active systems were prepared by the polymerization of conducting polymer layers on the surface of porous PVDF films as supports. During the preparation of PVDF supports the formation of pores during uniaxial extension is accompanied by the development of a pronounced relief on the film surface. This important effect is due to the structure transformation: it is the relief that provides a high adhesion of conducting polymer layers to the support. Owing to the orientation efforts during uniaxial extension the polymorphous transition of PVDF crystals into a piezo-active form also goes at this stage in parallel with the formation of pores. As a result, the prepared films

and the composites based on them are characterized by a unique combination of a porous structure and high content of a piezo-active β-phase. Electric properties of the deposited conducting polymer coatings on the surface of a PVDF support make it possible to use them as electrodes for polarization and measurements of the piezo modulus in the composites. It should be noted that the homogeneous layers of the rigid-chain of conducting polymers make composites mechanically stable during deformation. The very important advantage of the elaborated approach is the ability to produce complete ready-to-use polymer-based piezo elements. Physical and functional characteristics of the prepared composites make them a promising piezoelectric material that may find an application in energy transducers, biosensors and actuators.

References

Bar-Cohen, Y., Zhang, Q. (2008) Electroactive polymer actuators and sensors. *MRS Bulletin*, 33 (3), 173–181. https://www.doi.org/10.1557/mrs2008.42 (In English)

Branciforti, M. C., Sencadas, V., Lanceros-Mendez, S., Gregorio Jr., R. (2007) New technique of processing highly oriented poly(vinylidene fluoride) films exclusively in the β phase. *Journal of Polymer Science: Part B: Polymer Physics*, 45 (19), 2793–2801. https://www.doi.org/10.1002/polb.21239 (In English)

Boinovich, L. B, Emelyanenko, A. M. (2008) Hydrophobic materials and coatings: Principles of design, properties and applications. *Russian Chemical Reviews*, 77 (7), 583–600. https://www.doi.org/10.1070/RC2008v077n07ABEH003775 (In English)

Chang, Y. M., Lee, J. S., Kim, K. J. (2007) Heartbeat monitoring technique based on corona-poled PVDF film sensor for smart apparel application. *Solid State Phenomena*, 124–126, 299–302. https://www.doi.org/10.4028/www.scientific.net/ssp.124-126.299 (In English)

Dang, Z.-M., Yuan, J.-K., Yao, S.-H., Liao, R.-J. (2013) Flexible nanodielectric materials with high permittivity for power energy storage. *Advanced Materials*, 25 (44), 6334–6365. https://www.doi.org/10.1002/adma.201301752 (In English)

Dmitriev, I. Yu., Kuryndin, I. S., Lavrentyev, V. K., Elyashevich, G. K. (2017) Structure and piezoelectric properties of microporous polyvinylidene fluoride films. *Physics of the Solid State*, 59 (5), 1041–1046. https://www.doi.org/10.1134/S1063783417050092 (In English)

Elyashevich, G. K., Kuryndin, I. S., Rosova, E. Yu. (2002) Composite membranes with conducting polymer microtubules as new electroactive and transport systems. *Polymers Advanced Technologies*, 13 (10–12), 725–736. https://www.doi.org/10.1002/pat.251 (In English)

Elyashevich, G. K., Kuryndin, I. S., Dmitriev, I. Yu. et al. (2019) Orientation efforts as regulatory factor of structure formation in permeable porous poly(vinylidene fluoride) films. *Chines Journal of Polymer Science*, 37 (12), 1283–1289. https://www.doi.org/10.1007/s10118-019-2284-2 (In English)

Gerasimov, D. I., Kuryndin, I. S., Lavrentyev, V. K. et al. (2020) Piezoelectric properties of the oriented porous poly(vynilidene) fluoride films. *AIP Conference Proceedings*, 2308 (1), article 030001. https://www.doi.org/10.1063/5.0033693 (In English)

Gerhard-Multhaupt, R. (2002) Less can be more. Holes in polymers lead to a new paradigm of piezoelectric materials for electret transducers. *IEEE Transactions on Dielectrics and Electrical Insulation*, 9 (5), 850–859. https://www.doi.org/10.1109/TDEI.2002.1038668 (In English)

Lebrun, L., Guyomar, D., Guiffard, B. et al. (2009) The characterisation of the harvesting capabilities of an electrostrictive polymer composite. *Sensors and Actuators A: Physical*, 153 (2), 251–257. https://www.doi.org/10.1016/j.sna.2009.05.009 (In English)

Liu, F., Awanis Hashim, N., Liu, Y. et al. (2011) Progress in the production and modification of PVDF membranes. *Journal of Membrane Science*, 375 (1–2), 1–27. https://www.doi.org/10.1016/j.memsci.2011.03.014 (In English)

Merlini, C., Barra, G. M. O., Araujo, T. M. et al. (2014) Electrically pressure sensitive poly(vinylidene fluoride)/polypyrrole electrospun mats. *RSC Advances*, 4 (30), 15749–15758. https://www.doi.org/10.1039/c4ra01058b (In English)

Ozkorucuklu, S. P., Kamile, Ö., Esengül, K. (2012) Preparation and transport properties of PPy/PVDF composite membrane. *Polymers Advanced Technologies*, 23 (8), 1202–1206. https://www.doi.org/10.1002/pat.2030 (In English)

Salimi, A., Yousefi, A. A. (2003) Analysis method: FTIR studies of β-phase crystal formation in stretched PVDF films. *Polymer Testing*, 22 (6), 699–704. https://www.doi.org/10.1016/S0142-9418(03)00003-5 (In English)

Yarysheva, A. I., Bagrov, D. V., Rukhlya, E. G. et al. (2012) Features of the delocalized crazing of high-density polyethylene in poly(ethylene oxide) solutions. *Polymer Science. Series A*, 54 (10), 779–786. https://www.doi.org/10.1134/S0965545X12090106 (In English)

Theoretical Physics. Cosmology

UDC 524.8 https://www.doi.org/10.33910/2687-153X-2021-2-1-33-40

The nature of the naked singularity in generalized Vaidya spacetime and white hole geodesics

V. D. Vertogradov[✉1, 2]

[1] Herzen State Pedagogical University of Russia, 48 Moika Emb., Saint Petersburg 191186, Russia
[2] Special Astrophysical Observatory of the Russian Academy of Sciences,
St Petersburg branch, 65 Pulkovskoe Rd, Saint Petersburg 196140, Russia

Author

Vitalii D. Vertogradov, ORCID: 0000-0002-5096-7696, e-mail: vdvertogradov@gmail.com

For citation: Vertogradov, V. D. (2021) The nature of the naked singularity in generalized Vaidya spacetime and white hole geodesics. *Physics of Complex Systems*, 2 (1), 33–40. https://www.doi.org/10.33910/2687-153X-2021-2-1-33-40

Received 4 December 2020; reviewed 30 December 2020; accepted 6 January 2021.

Funding: This work was supported by RFBR grant No. 18-02-00461.

Abstract. This paper gives conditions to the energy-momentum tensor when the gravitational collapse of generalized Vaidya spacetime results in a naked singularity. We also consider the gravitational collapse of a matter cloud whose interior is described with Vaydia-de Sitter spacetime—when the collapse ends, this metric must be the de Sitter one, and the result of such a collapse is a so-called regular black hole. We provide the geodesic equations for the case when the matter is described with the equation of the state both $P = -\rho$ and $P = \alpha\rho$, where α belongs to the interval $\left(0, \frac{1}{3}\right]$. We match these geodesics with geodesics in the Schwarzschild metric. We also explain the nature of white hole geodesics with either the naked singularity formation or the regular black hole formation.

Keywords: generalized Vaidya spacetime, naked singularity, geodesics, matching, white hole geodesics, black hole.

Introduction

The problem of gravitational collapse is one of the most interesting in modern theoretical physics. In 1939, Oppenheimer and Snyder (Oppenheimer, Snyder 1939) built a model of the gravitational collapse with the assumption of the pressureless matter. For a long time, a black hole was considered to be the inevitable result of the gravitational collapse. However, it was shown that the gravitational collapse might also result in a naked singularity (see (Joshi 2007; Joshi, Malafarina 2011)). The naked singularity forms when the time of the singularity formation during the gravitational collapse is less than the time of the apparent horizon formation, and there must be a family of non-spacelike, future-directed geodesics which terminate at the central singularity in the past. It should be noted that the existence of only a family of non-spacelike geodesics is not sufficient for a naked singularity formation. It was shown (Grib et al. 2014; Vertogradov 2015) that all geodesics for particles with negative energy in the ergosphere of a rotating black hole appear in the ergosphere from the region inside the gravitational radius. In particular, it was shown that all null geodesics for such particles originate at the singularity of the Kerr black hole. And this statement is valid for geodesics for particles with positive energy (but not for all) (Grib, Pavlov 2015). However, in the case when $a \neq 1$ (i.e., a non-critical black hole), the Kerr black hole is not a naked singularity. If we can prove only the existence of a family of non-spacelike geodesics, then the result of a gravitational collapse might be a white hole. But, in the case of white hole, it takes infinite time to get to the external observer, because a white hole has the apparent horizon. It is worth mentioning that a naked singularity formation violates cosmic censorship conjecture (CCC) which states that all

singularity must be covered with a horizon. However, Papapetrou (Papapetrou 1985) was the first who showed the violation of CCC, and the Vaidya spacetime was one of the earliest counter examples of CCC. The generalized Vaidya spacetimes have been widely used in the studies of dynamical black holes (Dawood, Ghosh 2004)), black holes with trapped regions, and the gravitational collapse (Brassel, Goswami, Maharaj 2017; Brassel, Maharaj, Goswami 2017).

Recently, Maharaj (Mkenyeleye et al. 2014) has shown that the result of the gravitational collapse of generalized Vaidya spacetime might be the naked singularity and the result of this collapse depends on the mass function $M(v,r)$, where v is advanced Eddington time. The conditions on the mass function, when the result of such a collapse is a naked singularity, were given in our earlier paper (Vertogradov 2016). Further, it was shown that this kind of singularity might be gravitationally strong (Nolan 1999; Tipler 1977). An interesting question arises: what matter is required in order for a nacked singularity to be formed? To answer this question, the expression of the energy-momentum tensor was investigated, and it was shown that a naked singularity might be formed when type II of matter field (Hawking, Ellis 1973) dominates in the center of the collapsing matter cloud.

There is also another interesting question regarding the nature of white hole geodesics. According to geodesics completeness, there must be geodesics which appear in our universe from a region which is located inside the gravitational radius. For example, these geodesics can be the ones for particles with negative energy in the Kerr metric (Grib et al. 2014; Vertogradov 2015), or the ones which describe the motion of an object from the point of rest to the region inside the event horizon. In order to investigate this question, we should consider the past of such geodesics. But black holes are not eternal and, to extend our geodesics into the past, we should consider the gravitational collapse. The nature of white hole geodesics might be either a naked singularity formation during the gravitational collapse or regular black holes (Dymnikova 1992; Dymnikova 2002). In the latter case, the geodesics do not terminate at the singularity in the past, and they come from the infinity but, due to high negative density, turn back to our world. In this aim, we consider the gravitational collapse of the matter cloud whose interior is described with Vaydia—de Sitter spacetime, and whose exterior, with the Schwarzschild one. Also we write down geodesics in this metric and geodesics with the mass function $M(v,r)=C(v)+D(v)r^{1-2\alpha}$ (Vertogradov 2016). Unfortunately, when we have to deal with generalized Vaidya spacetime, we must consider a thin matter layer between two solutions—the generalized Vaidya spacetime and the Schwarzschild one. This is because the generalized Vaidya spacetime in which the mass function M does not depend on the time v is the Schwarzschild spacetime plus some extra term which we can define from the equation of the state. So we cannot smoothly match the generalized Vaidya spacetime with the Schwarzschild metric. In order to explain the nature of a so-called white hole geodesic in the Schwarzschild metric, we will use the usual Vaidya metric when the mass function $M = M(v)$ is the function of time only.

In sec. "Energy momentum tensor in the case of a naked singularity formation" we consider the energy-momentum tensor in the case of the naked singularity formation. In sec. "Vaydia—de Sitter spacetime", we consider the Vaydia—de Sitter metric. In sec. "Matching", we write down geodesics in the generalized Vaidya spacetime and the usual Vaiday spacetime and match them to the Schwarzschild ones.

The system of units $c = G = 1$ will be used throughout the paper. Dash and overdot denote partial derivative with respect to coordinates r and v respectively.

Energy momentum tensor in the case of a naked singularity formation

In the general case, the generalized Vaidya spacetime is given by:

$$\begin{aligned} ds^2 &= -\left(1-\frac{2M\left(v,r\right)}{r}\right)dv^2+2\epsilon dvdr+r^2d\Omega^2, \\ d\Omega^2 &= d\theta^2+\sin^2\theta d\varphi^2, \\ \epsilon &= \pm 1, \end{aligned} \tag{1}$$

where $M(v,r)$ is the mass function.

In this paper we consider the energy-momentum tensor which is the combination of types I and II of matter fields (Hawking, Ellis 1973). Here type II of the matter field represents so-called null dust with the energy density μ, and type I is the cosmic strings. In the case of metric (1), by virtue of the Einstein field equations, the energy-momentum tensor has the form (Wang, Wu 1999):

 https://www.doi.org/10.33910/2687-153X-2021-2-1-33-40

$$T_{\mu\nu} = T^{(m)}_{\mu\nu} + T^{(n)}_{\mu\nu} \ , \tag{2}$$

where $T^{(m)}_{\mu\nu}$ and $T^{(n)}_{\mu\nu}$ correspond to types I and II of matter fields respectively.
Now we write down the explicit form of the energy-momentum tensor:

$$\begin{aligned}
&T^{(n)}_{\mu\nu} = \mu L_\mu L_\nu \ , \\
&T^{(m)}_{\mu\nu} = \left(\rho + P\right)\left(L_\mu N_\nu + L_\nu N_\mu \right) + g_{\mu\nu} P \ , \\
&\mu = \frac{2\dot{M}}{r^2} \ , \\
&\rho = \frac{2M'}{r^2} \ , \\
&P = -\frac{M''}{r} \ , \\
&L_\mu = \delta^0_\mu \ , \\
&N_\mu = \frac{1}{2}\left(1 - \frac{2M}{r}\right)\delta^0_\mu - \varepsilon\delta^1_\mu \ , \\
&L_\mu L^\mu = N_\mu N^\mu = 0 \ , \\
&L_\mu N^\mu = -1 \ .
\end{aligned} \tag{3}$$

Here P is the pressure, ρ is the density and L^μ, n^μ are two null vectors. One should also distinguish the null dust energy density μ, which is the function, and subscript μ which takes values {0, 1, 2, 3}.

Our earlier paper (Vertogradov 2016) gives conditions for the mass function when the result of collapse is a naked singularity. The matter must satisfy the equation of the state $P = \rho\alpha$, where α belongs to the interval $\left(0, \frac{1}{3}\right]$. In this case, the mass function is given by:

$$M\left(v, r\right) = C\left(v\right) + D\left(v\right) r^{1-2\alpha} \ , \tag{4}$$

where C and D are two arbitrary functions of v only. Our model must be physically reasonable, and the energy-momentum tensor must satisfy energy conditions (Poisson 2004). Due to this conditions, we have the following restrictions on the mass function:

$$\begin{aligned}
&C\left(0\right) = 0 \ , \ D\left(0\right) \geq 0 \ , \ \dot{C}\left(v\right) \geq 0 \ , \\
&\dot{C}\left(v\right) + \dot{D}\left(v\right) r^{1-2\alpha} > 0 \ .
\end{aligned} \tag{5}$$

Now, substituting 4 into 3, we obtain:

$$\begin{aligned}
T_{00} &= \left(\frac{2\dot{C}\left(v\right) + \dot{D}\left(v\right) r^{1-2\alpha}}{r^2}\right)^{(n)} + \\
&+ \left[\left(1 - \frac{2C\left(v\right) + 2D\left(v\right) r^{1-2\alpha}}{r}\right)\frac{2\left(1-2\alpha\right)D\left(v\right)}{r^{1+2\alpha}}\right]^{(m)} \ , \\
T_{01} &= -\rho = -\frac{2\left(1-2\alpha\right)D\left(v\right)}{r^{1+2\alpha}} \ , \\
P &= \frac{2\alpha\left(1-2\alpha\right)D\left(v\right)}{r^{1+2\alpha}} \ .
\end{aligned} \tag{6}$$

Here symbols *n, m* correspond to types I and II of matter fields respectively.

The singularity is formed at $v = 0$, $r = 0$. The necessary condition for a singularity to be naked (Vertogradov 2016) is $D(0) = 0$. Substituting this condition into (6), we find that the part of the energy momentum tensor which corresponds to type I of the matter field vanishes throughout except for the center at $r = 0$ in this case. Thus, the singularity can be naked only when $T_{\mu\nu}^{(m)} = 0$. If $T_{\mu\nu}^{(m)} \neq 0$, the apparent horizon is formed and the singularity stops to be naked.

If we take into account quantum effects, a naked singularity can exist in the present of type I of the apparent horizon, but its formation is still temporary, and in short time the apparent horizon is formed, and the singularity becomes covered with the horizon.

So, in this case, a naked singularity is formed only if type I of the matter field is present at the singularity—then there is the level $0 < r \leq r_{II}$ which purely contains of type II of the matter field (here r_{ii} corresponds to the end of this level). So we must find out the solution of Einstein equations for this level, then we must match this new solution with the generalized Vaidya solution at $r = r_{ii}$.

The Einstein tensor in the case of generalized Vaidya spacetime has components:

$$\begin{aligned} G_{00} &= \frac{(2M - r)M'' + 2\dot{M}}{r^2} + \frac{1}{2}\left(1 - \frac{2M}{r}\right)\left(\frac{2M'}{r} + \frac{4M'}{r^2}\right), \\ G_{01} &= -\frac{2M'}{r^2}, \\ G_{22} &= -2rM', \\ G_{33} &= \sin^2\theta G_{22}. \end{aligned} \tag{7}$$

From (3) we see that in the case of type II of the matter field we have only one non-vanishing component of energy-momentum tensor—that is, T_{00}. Hence, from the fact that $G_{01}=T_{01}=0$, we obtain:

$$\begin{aligned} 2\frac{2M'}{r^2} &= 0, \\ M &= M(v). \end{aligned} \tag{8}$$

So the level $0 < r \leq r_{II}$ is described with the Vaidya metric.

In this case, at the border $r = r_{ii}$ of the two levels we must have:

$$M(v) = C(v) + D(v)r_{II}^{1-2\alpha}. \tag{9}$$

Vaydia—de Sitter spacetime

The expressions for the density and the pressure in the case of generalized Vaidya spacetime have the form:

$$\begin{aligned} \rho &= \frac{2m'}{r^2}, \\ P &= -\frac{m''}{r}. \end{aligned} \tag{10}$$

We are interested in the equation of the state:

$$P = -\rho. \tag{11}$$

In this case the mass function has the form:

$$m(v, r) = c(v) + d(v)r^3. \tag{12}$$

The exterior metric after collapse must be the de Sitter one. The first requirement for this is:

$$c(v) = 0. \tag{13}$$

If we cannot satisfy this condition, then the metric will have singularity at $r = 0$, and, as a result, it will not be the de Sitter one.

 https://www.doi.org/10.33910/2687-153X-2021-2-1-33-40

Then, at the time $v = v_{end}$, when the gravitational collapse stops, the following condition must be met:

$$d\left(v_{end}\right) = \frac{\lambda}{6} . \tag{14}$$

Here λ is the cosmological constant.

The equation of the apparent horizon in this case is given by:

$$r = \frac{1}{d\left(v\right)} . \tag{15}$$

The Vaydia—de Sitter spacetime is matched with the Schwarzschild one at the boundary of the collapsing cloud $r = r_b$, and following conditions must be satisfied:

$$\begin{gathered} d\left(v\right) r_b^3 = M = const , \\ dv = dt + \frac{1}{1 - \frac{2M}{r}} dr . \end{gathered} \tag{16}$$

As seen from (16), we have a narrow class of functions to match these metrics, because we cannot smoothly match geodesics at the boundary of the two metrics. Because $\frac{d}{dr}\left(D(v) r^3\right)|_{r=r_b} \neq 0$, as in the case of Schwarzschild spacetime when $\frac{dM}{dr} = 0$, there must be a thin matter layer between these spacetimes which smoothly matches to both metrics.

Let us consider the region $0 < r < r_{VD}$ which is described by Vaydia-de Sitter spacetime. r_{VD} is the boundary of this metric. We know that the metric of this region is:

$$ds_{DV}^2 = -\left(1 - 2\, d\left(v\right) r^2\right) dv^2 + 2 dv dr + r^2 d\Omega^2 . \tag{17}$$

Now let us consider a family of radially null geodesics in this metric. We can write:

$$\frac{dv}{dr} = \frac{2}{1 - d\left(v\right) r^2} . \tag{18}$$

The apparent horizon in this metric is given by:

$$r_{AH} = \sqrt{\frac{1}{2d\left(v\right)}} . \tag{19}$$

Also we must notice that the expansion is positive inside the apparent horizon and negative, outside it. The expansion θ in this case is written by:

$$e^{-\gamma} \theta = \frac{2}{r^2} \left(1 - 2d\left(v\right) r^2\right) , \tag{20}$$

where the factor $e^{-\gamma}$ does not any impact on the sign of the expansion.

Now, if we assume that $r_{AH} < r_{VD}$, we can consider a geodesic which originates at the infinity in Schwarzschild spacetime and then crosses the boundary of the collapsing cloud whose interior is described by the Vaydia—de Sitter metric. Now let us look at the equation (18): we will notice that this geodesic cannot cross the apparent horizon because in this case $\frac{dv}{dr}$ must be negative (we require only forward motion in time), but inside the apparent horizon $\frac{dv}{dr}$ is always positive. If $r_{AH} \geq r_{VD}$, then the geodesic has a turning point inside the thin matter layer because it cannot cross the hypersurface $r = r_{VD}$. If such a geodesic then goes to Schwarzschild spacetime, then this geodesic becomes a white hole geodesic in Schwarzschild spacetime.

Matching

We begin our consideration with the simplest case of radial null geodesics. In Schwarzschild spacetime, radial null geodesics are given by:

$$\frac{dt}{dr} = \pm \frac{1}{1 - \frac{2M}{r}} \,. \tag{21}$$

Radial null geodesics in the case of generalized Vaidya spacetime with the mass function $M(v,r) = C(v)+D(v)r^{1-2\alpha}$ are given by:

$$\frac{dv}{dr} = \frac{2r}{r - C(v) - D(v) r^{1-2\alpha}} \,. \tag{22}$$

Now by putting that at the boundary of collapsing cloud $r = r_b$:

$$C(v) + D(v) r_b^{1-2\alpha} = M = const \,, \tag{23}$$

by substituting (23) into (22), and by doing the following transformation:

$$dv = dt + \frac{dr}{1 - \frac{2M}{r}} \,, \tag{24}$$

we finally obtain:

$$\frac{dt}{dr} = \frac{1}{1 - \frac{2M}{r}} \,. \tag{25}$$

And we see that (25) coincides with (21).

If we consider the general case, then we should also demand that:

$$\lim_{r \to r_b} (1 - 2\alpha) \frac{D(v)}{r^{2\alpha}} = 0 \,. \tag{26}$$

The condition (26) can be satisfied if $\alpha > 0$ and $r_b >> D(v)$. In particular, we can smoothly match geodesics in Vaydia—de Sitter spacetime to geodesics in the Schwarzschild one.

The condition (26) appears due to the geodesic equation. In fact, that geodesics in Vaidya spacetime involve the first derivative of the mass function $M(v,r)$ with respect to the coordinate r, and it is not equal to zero like in the Schwarzschild case.

If we want the gravitational collapse of generalized Vaidya spacetime to result in a regular black hole, then we should consider three regions of spacetime:

1) The Vaydia—de Sitter spacetime when $0 < r < r_c$, where $r_c < r_b$;
2) The generalized Vaidya spacetime with the mass function $M(v,r) = C(v) + D(v)r^{1-2\alpha}$ when $r_c < r < r_b$;
3) The Schwarzschild spacetime when $r > r_b$;

To match region II to region III, we should satisfy conditions (23) and (26). To match region I to region II, the following conditions must be met:

$$\begin{aligned} &D_i(v) r_c^3 = C_{ii}(v) + D_{ii}(v) r_c^{1-2\alpha}, \;\; 3D_i(v) r_c^2 = (1 - 2\alpha) D_{ii}(v) r_c^{2\alpha}, \\ &r_c < r_b \,. \end{aligned} \tag{27}$$

Here I and II denote I and II regions respectively. If we are able to satisfy conditions (23), (26) and (27), then the gravitational collapse might result in a regular black hole.

Unfortunately, with the equation of the state $P = \alpha\rho$, where α is a real number, we always have the approximation (26). To remove it, we should consider a more complex equation of the state.

Finally, we provide geodesics in both Vaydia—de Sitter spacetime and generalized Vaidya spacetime with the mass function $M(v,r) = C(v) + D(v)r^{1-2\alpha}$, where $0 < \alpha \leq \frac{1}{3}$ in terms of the mass function $M(v,r)$. They are:

 https://www.doi.org/10.33910/2687-153X-2021-2-1-33-40

$$\frac{d^2v}{d\tau^2}+\frac{M-M'r}{r^2}\left(\frac{dv}{d\tau}\right)^2-r\left(\frac{d\theta}{d\tau}\right)^2-r\sin^2(\theta)\left(\frac{d\varphi}{d\tau}\right)^2=0\,,$$

$$\frac{d^2r}{d\tau^2}+\frac{\left(1-\frac{2M}{r}\right)(M-M'r)+r\dot{M}}{r^2}\left(\frac{dv}{d\tau}\right)^2$$

$$+2\frac{rM'-M}{r^2}\frac{dv}{d\tau}\frac{dr}{d\tau}+(2M-r)\left(\frac{d\theta}{d\tau}\right)^2+(2M-r)\sin^2(\theta)\left(\frac{d\varphi}{d\tau}\right)^2=0\,, \qquad (28)$$

$$\frac{d^2\theta}{d\tau^2}+\frac{2}{r}\frac{dr}{d\tau}\frac{d\theta}{d\tau}-\sin(\theta)\cos(\theta)\left(\frac{d\varphi}{d\tau}\right)^2=0\,,$$

$$\frac{d^2\varphi}{d\tau^2}+\frac{2}{r}\frac{dr}{d\tau}\frac{d\varphi}{d\tau}+2ctg(\theta)\frac{d\varphi}{d\tau}\frac{d\theta}{d\tau}=0\,.$$

For example, if we consider only two regions (II and III) and the result of the gravitational collapse is a naked singularity, then a non-spacelike future-directed geodesic which originates at the singularity in the past crosses the boundary of the collapsing cloud and turns out to be a white hole geodesic in Schwarzschild spacetime.

Conclusion

In this paper, we considered the form of the energy-momentum tensor in the case of a nacked singularity formation. We found out that a naked singularity can be formed only if type II of the matter field dominates. As soon as the matter field of type I appears, the apparent horizon is formed and the singularity stops to be naked.

In order to consider the nature of white hole geodesics, we also considered the Vaydia—de Sitter metric and found out that we can match it to the Schwarzschild one. In order to obtain a regular black hole as a result of such a gravitational collapse, we should consider three regions which are described with Vaydia-de Sitter spacetime, generalized Vaidya spacetime with the mass function $M(v,r) = C(v) + D(v)r^{1-2\alpha}$ and Schwarzschild metric. In this case, a geodesic comes from the infinity but, due to high negative density inside the collapsing cloud matter, turns back to our universe. If the result of a gravitational collapse is a naked singularity, a non-spacelike future-directed geodesic originates at this singularity, crosses the boundary of the ball of collapsing matter, and turns out to be a white hole geodesic in Schwarzschild spacetime.

Of course, for a more realistic case, we should consider a more complex equation of the state and also take into account the rotation. A gravitational collapse of the matter cloud with small rotation is being considered now

Acknowledgments

The author extends his gratitude to Professor D.Ph.-M.Sc. A. A. Grib and Professor Pankaj Joshi for scientific discussion.

References

Brassel, B. P., Goswami, R., Maharaj, S. D. (2017) Collapsing radiating stars with various equations of state. *Physical Review D*, 95 (12), article 124051. https://www.doi.org/10.1103/PhysRevD.95.124051 (In English)

Brassel, B. P., Maharaj, S. D., Goswami, R. (2017) Diffusive and dynamical radiating stars with realistic equations of state. *General Relativity and Gravitation*, 49 (3), article 37. https://www.doi.org/10.1007/s10714-017-2202-2 (In English)

Dawood, A. K., Ghosh, S. G. (2004) Generating dynamical black hole solutions. *Physical Review D*, 70 (10), article 104010. https://www.doi.org/10.1103/PhysRevD.70.104010 (In English)

Dymnikova, I. (1992) Vacuum nonsingular black hole. *General Relativity and Gravitation*, 24 (3), 235–242. https://doi.org/10.1007/BF00760226 (In English)

Dymnikova, I. (2002) The cosmological term as a source of mass. *Classical and Quantum Gravity*, 19 (4), 725–740. https://www.doi.org/10.1088/0264-9381/19/4/306 (In English)

Grib, A. A., Pavlov, Yu. V. (2015) Are black holes totally black? *Gravitation and Cosmology*, 21 (1), 13–18. https://www.doi.org/10.1134/S0202289315010065 (In English)

Grib, A. A., Pavlov, Yu. V., Vertogradov, V. D. (2014) Geodesics with negative energy in the ergosphere of rotating black holes. *Modern Physics Letters A*, 29 (20), article 1450110. https://www.doi.org/10.1142/S0217732314501107 (In English)

Hawking, S. W., Ellis, G. F. R. (1973) *The large scale structure of space-time*. London: Cambridge University Press, 385 p. https://doi.org/10.1017/CBO9780511524646 (In English)

Joshi, P. S. (2007) *Gravitational collapse and spacetime singularities*. Cambridge: Cambridge University Press, 269 p. https://doi.org/10.1017/CBO9780511536274 (In English)

Joshi, P. S., Malafarina, D. (2011) Recent developments in gravitational collapse and spacetime singularities. *International Journal of Modern Physics D*, 20 (14), 2641–2729. https://www.doi.org/10.1142/S0218271811020792 (In English)

Mkenyeleye, M. D., Goswami, R., Maharaj, S. D. (2014) Gravitational collapse of generalized Vaidya spacetime. *Physical Review D*, 90 (6), article 064034. https://www.doi.org/10.1103/PhysRevD.90.064034 (In English)

Nolan, B. C. (1999) Strengths of singularities in spherical symmetry. *Physical Review D*, 60 (2), article 024014. https://www.doi.org/10.1103/PhysRevD.60.024014 (In English)

Oppenheimer, J. R., Snyder, H. (1939) On continued gravitational contraction. *Physical Review*, 56 (5), 455–459. https://www.doi.org/10.1103/PhysRev.56.455 (In English)

Papapetrou, A. (1985) Formation of singularity and causality. In: N. Dadhich (ed.). *A random walk in relativity and cosmology: Essays in honour of P C. Vaidaya and A. K. Raychaudhuri*. New York: Wiley Publ., pp. 184–191. (In English)

Poisson, E. (2004) *A relativist's toolkit: The mathematics of black-hole mechanics.* Cambridge: Cambridge University Press, 233 p. https://doi.org/10.1017/CBO9780511606601 (In English)

Tipler, F. J. (1977) Singularities in conformally flat spacetimes. *Physics Letters A*, 64 (1), 8–10. https://www.doi.org/10.1016/0375-9601(77)90508-4 (In English)

Vertogradov, V. D. (2015) Geodesics for particles with negative energy in Kerr's metric. *Gravitation and Cosmology*, 21 (2), 171–174. https://www.doi.org/10.1134/S0202289315020115 (In English)

Vertogradov, V. D. (2016) Naked singularity formation in generalized Vaidya space-time. *Gravitation and Cosmology*, 22 (2), 220–223. https://www.doi.org/10.1134/S020228931602016X (In English)

Wang, A., Wu, Y. (1999) LETTER: Generalized vaidya solutions. *General Relativity and Gravitation*, 31 (1), 107–114. https://www.doi.org/10.1023/A:1018819521971 (In English)

Astrophysics and Stellar Astronomy.
General Relativity and Gravity

UDC 551.46+53.09 https://www.doi.org/10.33910/2687-153X-2021-2-1-41-48

Tide level in time and frequency domains at Dili port: Characteristic feature of a Lorentz oscillator

A. F. Belo✉[1], K. Sasa[2], J. M. Marques[2], K. Shimakawa[3]

[1] East Timor National University, Av. Cidade de Lisboa, Díli, East Timor
[2] Dili Port Technical Authority, Edificio Central da APORTIL, Dili, East Timor
[3] Gifu University, 1–1 Yanagido, Gifu 501-1193, Japan

Authors
Abelito Filipe Belo, e-mail: abelitofilipe@gmail.com
Kenji Sasa
Jose Madeira Marques
Koichi Shimakawa

For citation: Belo, A. F., Sasa, K., Marques, J. M., Shimakawa, K. (2021) Tide level in time and frequency domains at Dili port: Characteristic feature of a Lorentz oscillator. *Physics of Complex Systems*, 2 (1), 41–48. https://www.doi.org/10.33910/2687-153X-2021-2-1-41-48

Received 18 January 2021; reviewed 28 January 2021; accepted 28 January 2021.

Abstract. Tide level during one year in time-domain measured at Dili port (East Timor) is analyzed by the frequency spectrum with the Fast Fourier Transform (FFT), together with the autocorrelation function (AF). The frequency spectrum shows a characteristic feature of the Lorentz-type resonance (Lorentz oscillator) with the special peaks which are attributed to the major tide constituents related to the gravitational motions of the sun and the moon. The Lorentz-type resonance occurs in water fluid systems under the periodic change in gravitational potential, which is similar to the electronic polarization under an electric potential change. The $1/f$ characteristics found at high frequencies in the power spectrum (the so-called $1/f$ characteristics in frequency domain) can be originated *only* from the gravitational effect, while its origin is usually discussed in terms of meteorology such as atmospheric pressure.

Keywords: tide level, fast Fourier transform (FFT), autocorrelation function, Lorentz oscillator, $1/f$ fluctuation.

Introduction

The tide level should have time-to-time variations (time domain), involving periodic cycles (Banno, Kuriyama 2012; Kleinhans et al. 2017; Pugh 1996) due to gravitational actions. Meteorological effects such as atmospheric pressure may induce a complexity in the tide level. A popular technique for analyzing tides is the harmonic analysis (HA) in time domain (TD), in which the series of N harmonic constituents (sinusoids) are assumed (Pawlowicz et al. 2002; Ro et al. 2007; Stephenson 2016). Constructing a histogram for the tide level should also be useful to know the probability density at a particular level (Murthy, Rahi 2014; Tomaselli et al. 2011). Another approach is to obtain a frequency spectrum (FS) in frequency domain (FD) (Franco 1997; Marone et al. 2013). The Fourier Transform (FT) is also a popular technique to obtain an FS (Banno, Kuriyama 2012).

In this study, we will principally discuss the FS of tide level at Dili Port (East Timor) that is located near the equator (8.55° S, 125.56° E). The study explores a minute-by-minute data from a one-year period. It should be mentioned that the studies on the tidal changes from the area near the equator are few. Here, we will only focus on gravitational effects, while the meteorological effects, in general, cannot be ignored (Andrade et al. 2018; Pugh 1996; Truccolo et al. 2006). It is shown that the tide levels are dominated

by four major gravitational constituents from the sun and the moon (M2, S2, K1, O1) and tide level dynamics is replicated well by the Lorentz-type resonance (Wooten 1972). The FS shows two principal peaks (diurnal and semidiurnal) (Ro 2007; Stewart 2008) and another constituent (one year), together with a 1/*f*-like characteristics at higher frequencies (Banno, Kuriyama 2012; Kogan 2008). It is also shown that the histogram of the tide level observed in time domain is approximated to be a Gaussian distribution function.

The autocorrelation function (AF) of the tide change clearly shows an equivalency to the Lorentz oscillator, suggesting that the tide flow resonates with the change of gravitational potentials. An analogy between the electronic polarization in microscopic media and the macroscopic tidal changes is of interest in complex systems in physics (Draper et al. 2014; Garrett, Cummins 2005). It is suggested, through this equivalency, that the 1/*f*-like nature originates only from the gravitational effect, while its origin is commonly attributed to a change in meteorology (Andrade et al. 2018).

Measurement system and analysis

Figure 1 shows the equipment instalation consisting of an ultrasonic system and a control circuit at Dili Port (Timor Leste) to which two of the authors are affiliated. This method is used to measure reflection between transmitting and receiving pulses of the ultrasonic wave. The pulses are controlled by the control circuit. The output pulse of the control circuit is converted and transferred to the Data Logger (DL). The DL performs the arithmetic processing of several signals from sensors which monitor the water level. The minute-by-minute annual data of the tide level are stored in the built-in memory and an SD card. The host device uses the RS-232C interface to communicate with the personal computer on which the "data processing software" is installed.

Fig. 1. Instalation of equipment consiting of an ultrasonic system and a control circuit at Dili Port (Timor Leste). *Fotografer: Author (Abelito Filipe Belo), 20 January 2021*

The DL-collected data are Fourier transformed (Fast Fourier Transform: FFT). The Fourier transform (FT) of a time-dependent function $f(t)$ is given by

$$F(f) = \int_{-\infty}^{\infty} f(t) e^{-i2\pi ft} dt , \quad (1)$$

where $F(f)$ is the Fourier spectrum and $|F(f)|^2$ is called the power spectrum, and f is the frequency (s^{-1}) (Kogan 2008; Papoulis 1962).

 https://www.doi.org/10.33910/2687-153X-2021-2-1-41-48

FFT is an algorithm that computes the discrete $F(f)$ (Zonst 2004). In general, a limited number (= 2^n) of discrete data, where n is an integer, is required to perform the FFT. We take the MATLAB programme that allows to remove this limitation and the minute-by-minute one-year period import data of the tide level (data number N = 544778) are Fourier transformed. The time interval of the data Δt is, therefore, given by t_p/N, where t_p is the period of measurement time. The frequency interval Δf is given as

$$\Delta f = \frac{1}{N\Delta t} \cdot \tag{2}$$

The autocorrelation function of a time-dependent series is the average measure of its time-domain properties, being average product of the signal $f(t)$ and a time-shifted version of itself, and is a function of the imposed time shift τ, i.e., $C(\tau) = \langle f(t)f(t+\tau)\rangle$ (Geng, Boufadel 2017; Kogan 2008). $C(\tau)$ is, therefore, useful for obtaining the information of the signal periodicity and its decay (loss of correlation), where τ is the correlation time. FT of $C(\tau)$ gives the power spectrum of $F(f)$, which is the well-known Wiener—Khintchine theorem (Kogan 2008):

$$\left|F\left(f\right)\right|^2 = 2\int_0^\infty \langle f\left(t\right) f\left(t+\tau\right)\rangle e^{-i2\pi f\tau} d\tau \tag{3}$$

Results and discussion

The tide level data at Dili Port (Timor Leste) were obtained for the period from May 2018 to July 2019. Note that the tide level is defined as the change from the chart datum level (CDL: minimum tide level is set to zero in one year). Figure 2 shows the measured time-dependent tide level $h(t)$ at every 1 minnute for one year. Amplitude modulation (AM)-like behavior (beat) is found, which is produced when two frequencies, f_1 and f_2, are close each other, i.e., the beat frequency is $f_1 - f_2$. The periodical time of the beat is, therefore, $1/(f_1 - f_2)$. Details on this issue with the harmonic analysis (HA) will be discussed later.

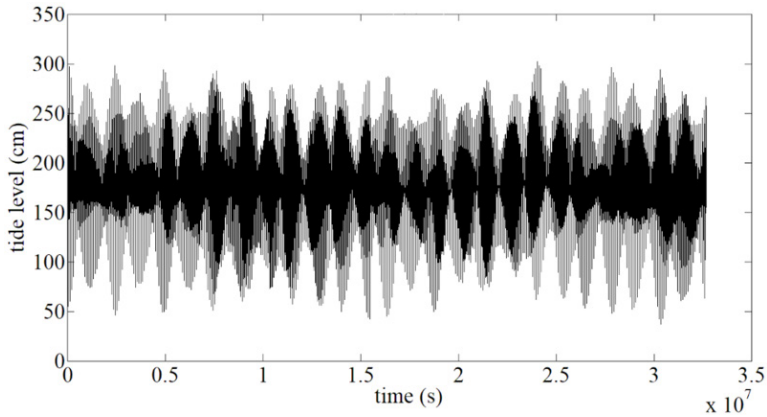

Fig. 2. Minute-by-minute one-year period data of the tide level

It may also be useful to show a histogram for the tide level h in which the probability density at a particular tide level can be obtained. The number of occurrences of each level is counted for this object. Discrete bars shown in Fig. 3 present the tide-level distribution for the total data set (N_T = 544778). It is found that the tide level follows a Gaussian distribution and is given by (Walpole et al. 2017):

$$G\left(h\right) = \frac{A}{\sqrt{2\pi\sigma^2}}\, exp\left\{-\frac{1}{2\sigma^2}\left(h-h_m\right)^2\right\}, \tag{4}$$

where A is a constant, σ is the standard deviation, and h and h_m are the tide level and its average, respectively.

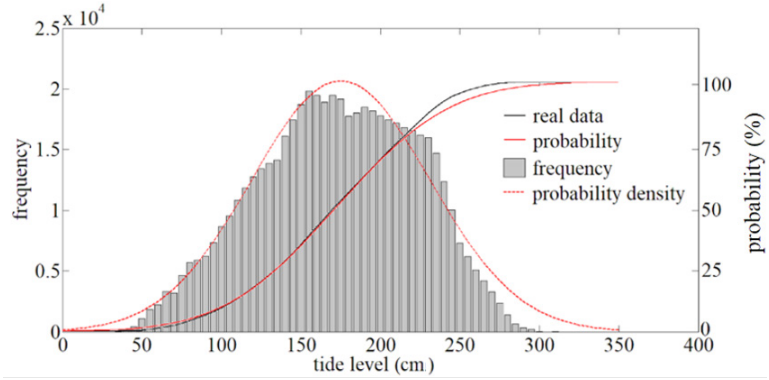

Fig. 3. Tide level distribution. Solid lines are predictions from the Gaussian (normal) distribution

The dashed line in Fig. 3 shows the probability density calculated from the $G(h)$ (A = 2.9 × 10^6, σ = 56, and h_m = 175). A more accurate comparison between the data and the probability distribution function should be given by an integral form of the histogram and the probability density, producing the probability only. Solid lines in Fig. 3 only show the probability calculated from the data (histogram) and the Gaussian distribution (red solid line) using the same parameters. Both curves fit well suggesting that the histogram basically follows a Gaussian distribution.

As is already stated, the discussion of the autocorrelation function $C(\tau)$ may be helpful to understand the underlying physics of the tide change, which produces information on the periodicity and keeps memory of the time of events (Kogan 2008). Figure 4 shows the autocorrelation functions of the practical tide for the imposed time shift, (a) τ_{max} = 30 days (2.59 × 10^6 s) and for (b) τ_{max} = one day (8.64 × 10^4 s). Here, we use the correlation time τ (not t) as a time variation. As seen for the $h(t)$ in Fig. 2, $C(\tau)$ shows the periodicity with beat. The time at which $C(\tau)$ is first crossing zero is a characteristic time τ_0 ($C(\tau_0) = 0$), which is a measure of the time of losing memory of an event and is estimated to be 1.25 × 10^4 s (~3.5 hr). The first (positive) peak at 4.54 × 10^4 s (~12.6 hr) and the second one at 8.96 × 10^4 s (~24.9 hr), respectively, are the mode frequencies of semidiurnal and diurnal changes in $h(t)$ (see also Fig. 2).

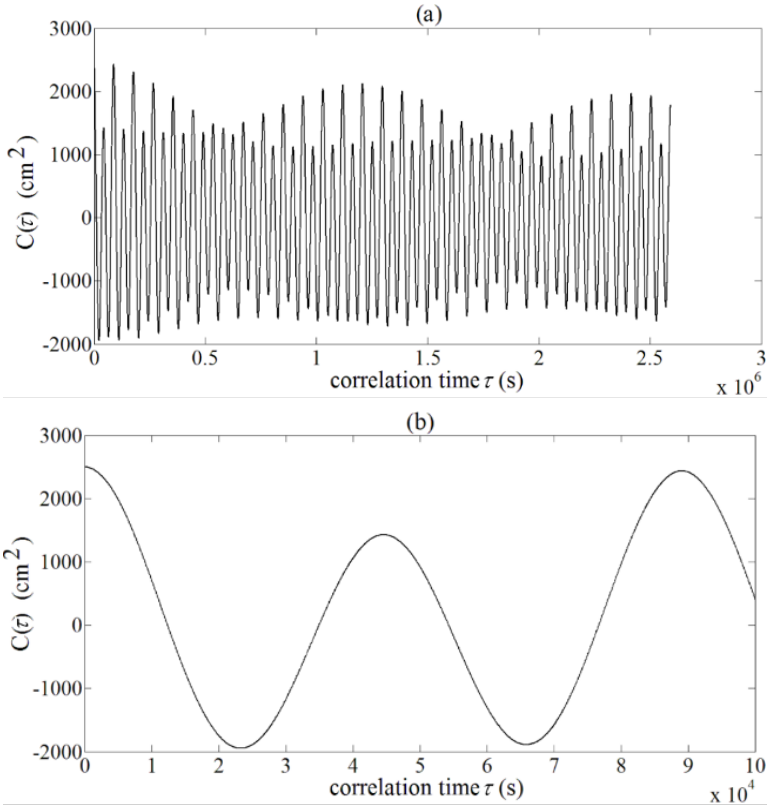

Fig. 4. Autocorrelation functions of the practical tide for (a) τ_{max} = one month, and for (b) τ_{max} = one day

 https://www.doi.org/10.33910/2687-153X-2021-2-1-41-48

These semidiurnal (M2 = 2.236 × 10^{-5} Hz, S2 = 2.315 × 10^{-5} Hz) and diurnal (K1 = 1.161 × 10^{-5} Hz, O1 = 1.076 × 10^{-5} Hz) modes can be attributed to the four major gravitational constituents from the sun and the moon. Magnitude of the semidiurnal mode is larger than the diurnal one (see Table 1).

Table 1. Standard values of relative amplitude and frequency for the semidiurnal (M2, S2) and diurnal (K1, O1) gravitational components of tide (Stewart 2008)

	Relative amplitude A_n	Frequency f_n (Hz)	Phase θ_n (rad)
M2	0.454	2.236 × 10^{-5}	–2.2
S2	0.212	2.315 × 10^{-5}	–1.6
K1	0.266	1.161 × 10^{-5}	0.0
O1	0.189	1.076 × 10^{-5}	–0.5

The beat periods related to the semidiurnal mode should be 1.27 × 10^6 s and to diurnal one, 1.18 × 10^6 s, which is consistent with the actual data shown in Fig. 2. The same beat periodicity on the $C(t)$ is found in Fig. 4 (a). The sinusoidal-like periodic response is similar to the Lorentz-type resonance in time domain, i.e.,

$$C(t) = Ae^{-\gamma t}\cos 2\pi f_0 t \ , \tag{5}$$

where A is the amplitude of displacement, γ the decay rate (s^{-1}), and f the frequency (Kogan 2008). The Lorentz-type displacement $Y(f)$ in frequency domain, i.e., the Fourier transform of $C(t)$, is known as (Kogan 2008; Wooten 1972)

$$Y(f) = \frac{B}{\left(f_0^{\,2} - f^2\right) - i\gamma f} \ , \tag{6}$$

where B is a constant, f_0 is the resonance frequency, and γ is the damping frequency (decay rate in time domain).

The solid (black) line (a) in Fig. 5 shows the power spectrum $|H(f)|^2$ ($cm^2\ Hz^{-1}$) obtained from the FFT of the time-variation of real tide $h(t)$ (practical data). The semidiurnal and diurnal peaks appear at ~2.3 × 10^{-5} Hz (peak 1) and 1.1 × 10^{-5} Hz (peak 2), respectively. Each peak splits into two peaks, producing the beats in $h(t)$ in time domain (see Fig. 2). Peaks 1 and 2, respectivey, are composed of the K_1 and O_1 and M_2 and S_2. The beats from the sets of (K_1,O_1) and (M_2 and S_2) are found in $h(t)$ shown in Fig. 2.

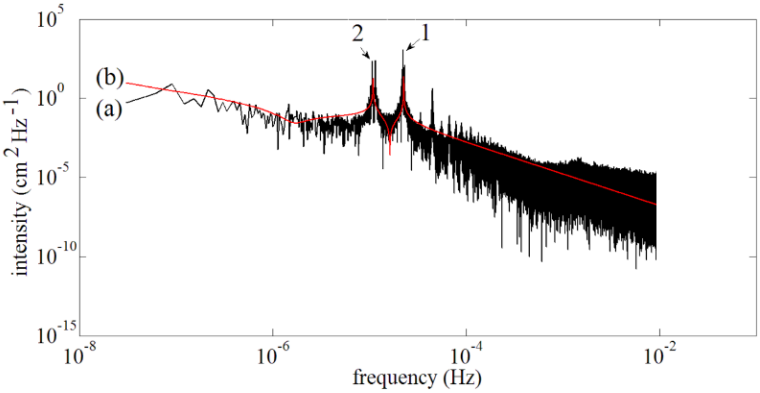

Fig. 5. Power spectrum of the tide level. Black solid line (a) is practical data; red line (b) is the model tide (Lorentz oscillators). 1 and 2 are the semidiurnal and diurnal peaks, respectively

Supposedly, the tidal change follows the Lorentz-type relaxation and the discussion in the frequency domain may clarify this point. Using eq. (5), the power spectrum $|H(f)|^2$ is approximated by|

$$\left|H(f)\right|^2 = \sum_{i=1}^{n} \frac{B_i}{\left(f_{0i}^{\,2} - f^2\right) - i\gamma_i f} \ , \tag{7}$$

where B_i is a constant, f_{0i} and γ_i is the resonant frequency and the damping frequency for i-th component, respectively. The solid line (b) shows the absolute intensity of the Lorentz oscillator (here $|H(f)|^2$) with the fitting parameters given in Table 2.

Table 2. Physical parameters for the Lorentz oscillators used for the fitting. C_i is the relative amplitude of B_i of the component (see text)

	f_{0i} (Hz)	B_i (cm² × Hz)	γ_i (Hz)	C_i
semidiurnal	2.28×10^{-5}	1.0×10^{-11}	1.0×10^{-8}	0.63
diurnal	1.10×10^{-5}	6.1×10^{-12}	1.0×10^{-8}	0.36
1 year	3.17×10^{-8}	2.0×10^{-13}	7.0×10^{-7}	0.01

For simplicity, we took one (average) frequency for the semidiurnal and dirnurnal peaks. At lower frequencies, in addition to these two peaks, we need another 3rd component (one-year periodicity) (Banno, Kuriyama 2012), since the $|H(f)|^2$ takes a constant value, without the 3rd component. Overall fitting of the Lorentz oscillator, including the 3rd constituent, to the practical data is reasonably good. At higher frequencies, we observe a decrease in the intensity with increasing frequency f, which is approximately proportional to $1/f^2$. This type of frequency-dependent behavior is similar to the $1/f$ noise or $1/f$ fluctuation (Kogan 2008). Note that the relative magnitudes of the Lorentz oscillator C_i in Table 2 are consistent with the relative intensity of the gravity constituents (M2 + S2, K1 + O1) (see Table 1).

Let us discuss tidal dynamics in more detail. It was shown that the power spectrum of the tide change was replicated well by the Lorentz oscillator. A popular example of the Lorentz oscillator (harmonic oscillation with damping) can be the dynamics of an electronic polarization, i.e., electronic displacement under a periodic electric field motion (complex dielectric function) (Wooten 1972) or a mechanical spring motion. For electronic displacement x under the external field F, the system follows Newton's second law as

$$M\frac{d^2x}{dt^2}+\gamma\frac{dx}{dt}+\omega_0^{\,2}x=F=Ae^{-i\omega_0 t} \quad , \tag{8}$$

where M is a mass (electronically charged), γ is the damping coefficient, and ω_0 is the angular resonant frequency (= $2\pi f_0$). The solution of the above equation under some conditions gives Eq. (5) or (6). When the second term in Eq. (8) is dominant, the Debye type dielectric relation dominates the system (no oscillation). Note also that the above resonant phenomena can be represented by an equivalent electrical circuit, i.e., *RLC* series connection (resonance circuit), where R is the resistance, L the inductance, and C the capacitance in the sense of electrical engineering (Kogan 2008; Prandle 1980). It was interesting to find out that the water fluid system under the periodic change in gravitational potential is phenomenologically the same as the electronic polarization under an electric potential change.

In addition to gravitational motion of the sun, the moon, and the earth, meteorology effects such as atmospheric pressure and wind power also contribute to the tide level (Andrade et al. 2018; Truccolo et al. 2006). Other contributing factors include the shape of the beach, coastline, and coastline depth (Kleinhans et al. 2017; Marone et al. 2013). While all these oceanic effects may dominate tidal behaviors, here we discuss the gravitational effect only. We once again suggest that the $1/f$-like nature at high frequencies originates gravitationally (nature of low-pass filter) without involving a meteorological effect.

Finally, we briefly discuss the harmonic analysis (HA) in time domain (Stewart 2008). We can model the series with I harmonic constituents of sinusoids (Stephenson 2016):

$$h(t)=H_0+C\sum_{i=1}^{I}A_n\cos\left(2\pi f_n t+\theta_n\right), \tag{9}$$

where A_n is the relative amplitude of the nth component (cm), f_n is the frequency (Hz), θ_n is the phase angle (rad), H_0 is the mean sea-level (cm) and C is the multicable constant (cm). In the present study, H_0 (= 180 cm), C (= 105 cm), and θ_n is taken as fitting parameters, while the major constituents (M2, S2, K1, O1) are taken as the tide wave of gravitational origin (I = 4) (see Table 1). Here, a one-year constituent (Matsumoto et al. 1995) was not involved in the HA. Comparisons of the actual tide change (black) with the model tide (red) are shown in Fig. 6 for the first one month. It is shown that the actual tide level is replicated well by the standard four parameters, M2, S2, K1, and O1 with some deviations.

 https://www.doi.org/10.33910/2687-153X-2021-2-1-41-48

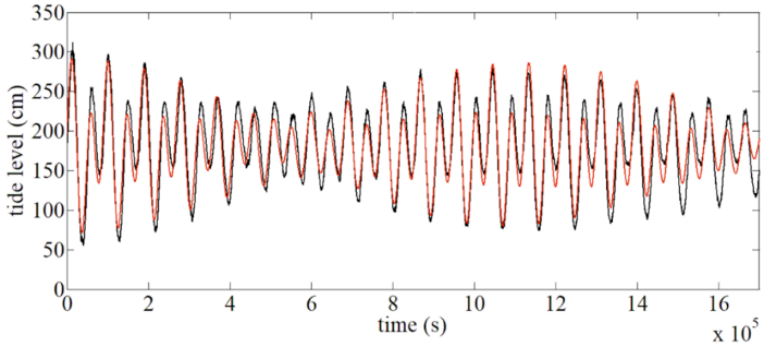

Fig. 6. Actual tide (black) and model tide (red) for the first one month

Conclusion

The minute-by-minute change in the tide level for a one-year period was measured at Dili port (East Timor). It was found that the histogram of the tide level in time-domain was approximated to be the Gaussian distribution function, with the mean height of 175 cm and the standard deviation of 56 cm. The frequency spectra through the Fast Fourier Transform (FFT) showed the two clear peaks (semidiurnal and diurnal) induced by the gravitational motions of the sun, the moon, and the earth. It was also suggested that the constituent of one-year dominated the power spectrum at low frequencies with no clear peak. The power spectrum was replicated well by the Lorentz oscillator, indicating that the tide flow resonates with the gravitational forces, which is phenomenologically the same as the electronic polarization under the electric field: *Microscopic dynamics spans to macroscopic one*. The spectrum shows the $1/f$ nature found at higher frequencies in the frequency spectra is a result of the Lorentz-type response. Origin of $1/f$ characteristics can therefore be attributed only to the gravitational effect without involving the meteorological one. It was shown by a harmonic analysis that the actual tide change was replicated well by the four standard gravitational parameters, M2, S2, K1, and O1. It was concluded that tidal behavior follows *nature's orders* even in *complex systems* of the globe.

Acknowledgments

We would like to thank Professor T. Kobayashi, Gifu University, for his useful contribution. We also wish to thank the JICA CADEFEST 2 for the financial support to the Faculty of Engineering, Universidade Nacional Timor Lorosa'e.

References

Andrade, M. M., Toldo, E. E., Nunes, J. C. R. (2018) Tidal and subtidal oscillations in a shallow water system in southern Brazil. *Brazilian Journal of Oceanography*, 66 (3), 245–254. https://doi.org/10.1590/s1679-87592018017406603 (In English)

Banno, M., Kuriyama, Y. (2012) The characteristic of shoreline response to cyclic tidal change. *Journal of Japan Society of Civil Engineers, Series B2 (Coastal Engineering)*, 68 (2), 576–580. https://www.doi.org/10.2208/kaigan.68.I_576 (In Japanese)

Draper, S., Adcock, T. A., Borthwick, A. G., Houlsby, G. T. (2014) An electrical analogy for the Pentland Firth tidal stream power resource. *Proceedings of the Royal Society A*, 470 (2161), article 20130207. https://www.doi.org/10.1098/rspa.2013.0207 (In English)

Franco, A. S. (1988) *Tides: fundamentals, analysis and prediction*. São Paulo: Fundação Centro Tecnológico de Hidráulica, 249 p. (In English)

Garrett, C., Cummins, P. (2005) The power potential of tidal currents in channels. *Proceedings of the Royal Society A: Mathematical, Physical and Engineering Sciences*, 461 (2060), 2563–2572. https://doi.org/10.1098/rspa.2005.1494 (In English)

Geng, X., Boufadel, M. C. (2017) Spectral responses of gravel beaches to tidal signals. *Scientific Reports*, 7, article 40770. https://www.doi.org/10.1038/srep40770 (In English)

Kleinhans, M. G., van der Vegt, M., Leuven, J. et al. (2017) Turning the tide: Comparison of tidal flow by periodic sea level fluctuation and by periodic bed tilting in scaled landscape experiments of estuaries. *Earth Surface Dynamics*, 5 (4), 731–756. https://www.doi.org/10.5194/esurf-5-731-2017 (In English)

Kogan, S. (2008) *Electronic noise and fluctuations in solids*. Cambridge: Cambridge University Press, 376 p. (In English)

Marone, E., Raicich, F., Mosetti, R. (2013) Harmonic tidal analysis methods on time and frequency domains: Similarities and differences for the Gulf of Trieste, Italy, and Paranaguá Bay, Brazil. *Bollettino di Geofisica Teorica ed Applicata*, 54 (2), 183–204. https://www.doi.org/10.4430/bgta0068 (In English)

Matsumoto, K., Ooe, M., Sato, T., Segawa, J. (1995) Ocean tide model obtained from TOPEX/POSEIDON altimetry data. *Journal of Geophysical Research: Oceans*, 100 (C12), 25319–25330. https://www.doi.org/10.1029/95JC02777 (In English)

Murthy, K. S. R., Rahi, O. P. (2014). Estimation of Weibull parameters using graphical method for wind energy applications. In: *2014 Eighteenth National Power Systems Conference (NPSC)*. Guwahati: IEEE Publ. [Online]. https://www.doi.org/10.1109/NPSC.2014.7103858 (accessed 10.01.2021). (In English)

Papoulis, A. (1962) *The fourier integral and its applications*. New York: McGraw-Hill Publ., 318 p. (In English)

Pawlowicz, R., Beardsley, B., Lentz, S. (2002) Classical tidal harmonic analysis including error estimates in MATLAB using T_TIDE. *Computers & Geosciences*, 28 (8), 929–937. https://www.doi.org/10.1016/S0098-3004(02)00013-4 (In English)

Prandle, D. (1980) Modelling of tidal barrier schemes: An analysis of the open-boundary problem by reference to AC circuit theory. *Estuarine and Coastal Marine Science*, 11 (1), 53–71. https://www.doi.org/10.1016/S0302-3524(80)80029-6 (In English)

Pugh, D. T. (1996) *Tides, surges and mean sea-level: A handbook for engineers and scientists*. Chichester: Wiley Publ., 472 p. (In English)

Ro, Y. J. (2007) Tidal and sub-tidal current characteristics in the Kangjin Bay, South Sea, Korea. *Ocean Science Journal*, 42 (1), 19–30. https://www.doi.org/10.1007/BF03020907 (In English)

Ro, Y. J., Jung, K. Y., Jun, W. S., Eom, H. M. (2007) Numerical modeling of tide and tidal current in the Kangjin Bay, South Sea, Korea. *Ocean Science Journal*, 42 (3), 153–163. https://www.doi.org/10.1007/BF03020919 (In English)

Stephenson, A. G. (2016) *TideHarmonics: Harmonic analysis of tides*. [Online]. Available at: https://cran.r-project.org/package=TideHarmonics (accessed 10.01.2021). (In English)

Stewart, R. H. (2008) *Introduction to physical oceanography*. [Online]. Available at: http://hdl.handle.net/1969.1/160216 (accessed 10.01.2021). (In English)

Tomaselli, P. D., Re, C. L., Ferreri, G. B. (2011) Analysis of tide measurements in a Sicilian harbour. In: H. Schüttrumpf, R. Tomasicchio (eds.). *5th SCACR 2011. International Short Conference on Applied Coastal Research*. Graz: Institute of Hydraulic Engineering and Water Resources Management Publ., pp. 579–586. (In English)

Truccolo, E. C., Franco, D., Schettini, C. A. F. (2006) The low frequency sea level oscillations in the northern coast of Santa Catarina, Brazil. *Journal of Coastal Research*, SI 39, 547–552. (In English)

Walpole, R. E., Myers, R. H., Myers, S. L., Ye, K. (2017) *Probability and statistics for engineers and scientists*. 9th ed. Singapore: Pearson Education South Asia Pte Ltd. Publ., 811 p. (In English)

Wooten, F. (1972) *Optical properties of solids*. New York: Academic Press, 272 p. https://doi.org/10.1016/C2013-0-07656-6 (In English)

Zonst, A. E. (2004) *Understanding the FFT applications: A tutorial for students & working engineers*. 2nd ed., rev. Titusville: Citrus Press., 182 p. (In English)